

Cohesive Zone-Based Damage Evolution in Periodic Materials Via Finite-Volume Homogenization

Wenqiong Tu

Civil Engineering Department,
University of Virginia,
Charlottesville, VA 22904-4742

Marek-Jerzy Pindera¹

Mem. ASME
Civil Engineering Department,
University of Virginia,
Charlottesville, VA 22904-4742

The zeroth-order parametric finite-volume direct averaging micromechanics (FVDAM) theory is further extended in order to model the evolution of damage in periodic heterogeneous materials. Toward this end, displacement discontinuity functions are introduced into the formulation, which may represent cracks or traction-interfacial separation laws within a unified framework. The cohesive zone model (CZM) is then implemented to simulate progressive separation of adjacent phases or subdomains. The new capability is verified in the linear region upon comparison with an exact elasticity solution for an inclusion surrounded by a linear interface of zero thickness in an infinite matrix that obeys the same law as CZM before the onset of degradation. The extended theory's utility is then demonstrated by revisiting the classical fiber/matrix debonding phenomenon observed in SiC/Ti composites, illustrating its ability to accurately capture the mechanics of progressive interfacial degradation. [DOI: 10.1115/1.4028103]

Keywords: micromechanics, homogenization, finite-volume method, damage, crack growth, fiber/matrix debonding

1 Introduction

Damage evolution in heterogeneous materials continues to receive considerable attention due to current emphasis on sustainability and efficiency in modern structural designs. The problem is a complex one due to the many local damage and failure mechanisms that occur in heterogeneous materials with large microstructure-induced stress fluctuations and gradients, including microcracks, phase debonding, and separation. Crack growth in such circumstances is typically non-self-similar, requiring continuous remeshing of the analysis domain within the variational framework, together with the application of an appropriate crack-growth criterion for the particular material system. To mitigate these complications, the CZM originally proposed by Barenblatt [1,2] for fracture of brittle materials, and subsequently extended by Dugdale [3] for perfectly plastic materials using the concept of a fracture process zone, has been adopted by numerous researchers to naturally track damage progression in heterogeneous materials. CZM is based on a traction-interfacial separation relation, which describes the interfacial degradation process between two adjacent phases or subdomains. This relation assumes that as the interface separates, traction first increases until the interfacial strength is reached and then decreases to zero, where complete separation occurs. The contributions of Needleman and coworkers [4,5] and Ortiz and coworkers [6,7] have spurred extensive use of CZM in simulating fracture phenomena in a wide range of material systems due to its demonstrated advantages of allowing spontaneous crack nucleation, crack branching, and fragmentation, as well as crack propagation without an external fracture criterion. Reviews of the different aspects and applications of CZM have been provided by Elices et al. [8], Jiang et al. [9], Banea and da Silva [10], Kim [11], and Park and Paulino [12] who discussed selection of appropriate cohesive laws for mixed-mode problems,

which ensure that certain combinations of interfacial tractions do not produce positive interfacial stiffness after the initiation of interfacial degradation.

The majority of CZM applications are based on variational techniques, especially the finite-element method. One convenient way to incorporate CZM into the finite-element framework is through cohesive or interface elements. By applying the principle of virtual work to the cohesive zone and carrying out finite-element discretization of the cohesive zone's upper and lower surfaces, displacements and corresponding tractions along these surfaces are connected at the discretized nodes through the local element stiffness matrix based on the chosen traction-interfacial separation relations and element shape functions. In heterogeneous materials, however, large modulus mismatch is often encountered, producing large stress gradients at phase interfaces. Therefore, in order to correctly simulate the crack opening and propagation process with CZM, convergence of both interfacial tractions and displacements requires extensive mesh refinement in the cohesive zone to ensure self-equilibrated stress fields upon minimization of total potential energy.

The finite-volume method has proved an attractive alternative to the established finite-element analysis of boundary-value problems in solid mechanics, cf. Berezovski et al. [13], following its original development focused on applications to fluid mechanics problems, Versteeg and Malalasekera [14]. In contrast with the variational techniques, local equilibrium within the finite-volume framework is satisfied in integral sense at the discretized subdomain level. The different variants of the method have been applied to a variety of elastic and inelastic boundary-value problems in the infinitesimal and finite-deformation domain, including fracture mechanics problems, cf. Ivankovic et al. [15], Ivankovic [16]. Following the success of CZM in finite-element applications, CZM has recently been implemented into the finite-volume framework, cf. Stylianou and Ivankovic [17], Karac et al. [18], and applied to study crack propagation along a bimaterial interface, Carolan et al. [19].

As discussed by Cavalcante et al. [20], three variants of the finite-volume method may be identified according to the manner of analysis domain discretization, subdomain field variable

¹Corresponding author.

Contributed by the Applied Mechanics Division of ASME for publication in the JOURNAL OF APPLIED MECHANICS. Manuscript received March 29, 2014; final manuscript received July 26, 2014; accepted manuscript posted July 30, 2014; published online August 13, 2014. Assoc. Editor: Nick Aravas.

approximation, and solution technique. In particular, the FVDAM theory was developed explicitly to simulate the response of heterogeneous materials with periodic microstructures, Pindera et al. [21]. The accuracy of homogenized and local responses has been shown to be comparable to the finite-element method with the added advantage that explicit relations between surface-averaged tractions and displacements are available through a local stiffness matrix that governs the equilibrated response of a subdomain, with the stiffness matrix elements available in closed form. These relations are derived directly from the assumed displacement field representation at the subdomain level following the elasticity approach without any additional assumptions. This circumvents the problem of accurate stress extrapolation to the subdomain surfaces encountered in finite-element and, until very recently, other finite-volume approaches, see Tukovic et al. [22] for a method of calculating displacement gradients at subdomain interfaces based on the cell-centered finite-volume method. The explicit analytical relations between interfacial tractions and interfacial displacements provide a natural way to incorporate CZM into the FVDAM framework absent in most other approaches. This and other features of FVDAM set it apart from the other versions of the finite-volume method, which are currently being applied to the CZM-based fracture analysis of heterogeneous materials, cf. Alveen et al. [23].

Herein, we extend the parametric FVDAM theory using a unified approach that allows simulation of both progressive phase separation based on CZM and crack growth within the same framework. To accomplish this, displacement discontinuity functions previously used in the solution of interfacial crack problems in multilayered materials, cf. Chen and Pindera [24], are introduced into the FVDAM framework. The discontinuity functions are obtained upon solution of auxiliary equations that represent either traction-free crack-face conditions, or interfacial degradation between phases governed by nonlinear traction-interfacial separation laws. The approach is first verified in the linear range upon comparison with an exact elasticity solution for the problem of an interface-clad cylindrical inclusion embedded in an infinite matrix under far-field unidirectional loading. The utility of the extended theory with implemented CZM capability is then demonstrated by revisiting the classical fiber/matrix debonding problem in SiC/Ti unidirectional composites.

2 Parametric FVDAM Theory With Evolving Damage

The parametric FVDAM theory is based on microstructural discretization of the unit cell of a periodic material into quadrilateral subvolumes generated by mapping a square-sided subvolume in reference coordinate system onto a quadrilateral subvolume in the actual microstructure. This mapping was first introduced by Cavalcante et al. [25] into the structural version of the finite-volume theory originally developed by Bansal and Pindera [26] to enable efficient modeling of complex microstructural details. Subsequently, the homogenized version had been constructed by Gattu et al. [27] and Khatam and Pindera [28,29] who introduced parametric mapping into the original rectangular subvolume-based FVDAM theory of Bansal and Pindera [30,31].

In contrast with the manner of incorporating CZM into the finite-element framework where nodal displacements are the basic unknowns, within the FVDAM framework the surface-averaged displacements at subvolume interfaces undergoing evolving damage are expressed as sums of continuous displacements and displacement discontinuities. The introduction of displacement discontinuities leads to two global systems of equations for the determination of the unknown continuous interfacial displacements and the introduced displacement discontinuities, herein called primary and auxiliary systems of equations. The primary system establishes the relations between continuous displacements and displacement discontinuities, with the number of equations in the primary system the same as in the corresponding global system without discontinuities. The additional equations come from

the auxiliary system, which relates the interfacial tractions of damaged or cracked interfaces to the corresponding displacement discontinuities. The explicit relations between interfacial tractions and displacements available through the local stiffness matrix formulation enable us to construct the auxiliary system of equations directly. This manner of reformulating the governing system of equations for the unit cell response provides two very attractive advantages. As already mentioned, the incorporation of CZM is straightforward due to the explicit traction-interfacial separation relations. Moreover, in order to obtain converged solutions for the displacement discontinuities, only the auxiliary system of equation needs to be solved iteratively, unlike the finite-element framework where the entire global system is solved at each load increment. The number of auxiliary equations is equal to the number of interfaces undergoing damage multiplied by the associated degrees of freedom. When this number is small compared to the total number of interfaces within the discretized unit cell, as in the case of interfacial debonding in fiber-reinforced materials, the auxiliary system of equations is also small facilitating very efficient solution.

2.1 Theoretical Framework. The unit cell's microstructure is discretized into quadrilateral subvolumes designated by the index (q) whose location is specified by the subvolume vertices $(y_2^{(p,q)}, y_3^{(p,q)})$. The q th quadrilateral subvolume is generated by mapping the reference subvolume in the $\eta-\xi$ plane bounded by $-1 \leq \eta \leq +1$ and $-1 \leq \xi \leq +1$ onto its actual location in the unit cell, Fig. 1, using the transformation

$$y_i^{(q)}(\eta, \xi) = \sum_{p=1}^4 N_p(\eta, \xi) y_i^{(p,q)}, \quad i = 2, 3 \quad (1)$$

where $N_1(\eta, \xi) = \frac{1}{4}(1 - \eta)(1 - \xi)$, $N_2(\eta, \xi) = \frac{1}{4}(1 + \eta)(1 - \xi)$, $N_3(\eta, \xi) = \frac{1}{4}(1 + \eta)(1 + \xi)$, and $N_4(\eta, \xi) = \frac{1}{4}(1 - \eta)(1 + \xi)$. Following the convention of Cavalcante et al. [25], the subvolume's vertices are numbered in counterclockwise manner starting from lower left corner $(y_2^{(1,q)}, y_3^{(1,q)})$. Accordingly, the faces are numbered counterclockwise with the face F_p defined by the endpoints $(y_2^{(p,q)}, y_3^{(p,q)})$ and $(y_2^{(p+1,q)}, y_3^{(p+1,q)})$ for $p = 1, 2, 3$, and 4 such that $p + 1 \rightarrow p$ when $p = 4$. The orientation of the face is defined by the unit normal $\mathbf{n}^{(p,q)} = [n_2^{(p,q)}, n_3^{(p,q)}]$ whose elements are defined by the vertex coordinates and the associated lengths.

Following the zeroth-order homogenization theory, cf. Bensoussan et al. [32], Suquet [33], and Charalambakis [34], the displacement field in the q th subvolume is represented by the two-scale expansion involving macroscopic and fluctuating components

$$u_i^{(q)}(\mathbf{x}, \mathbf{y}(\eta, \xi)) = \bar{e}_{ij}x_j + u_i^{(q)}(\eta, \xi) \quad (2)$$

The fluctuating displacements $u_i^{(q)}$ ($i = 1, 2$, and 3) are approximated by the second order, Legendre-type polynomial expansion

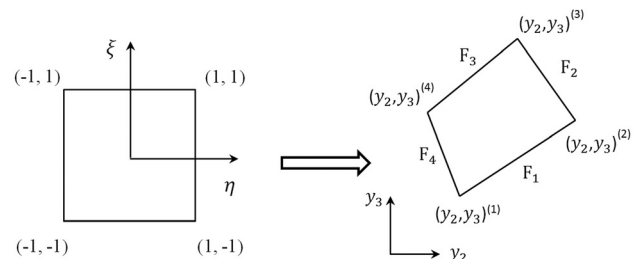


Fig. 1 A reference square subvolume in the $\eta-\xi$ plane (left) mapped onto a quadrilateral subvolume in the y_2-y_3 plane (right) of the actual microstructure

in the reference coordinates (η, ξ) consistent with the generalized plane strain constraint, which ensures that $\bar{\varepsilon}_{11} = \hat{\varepsilon}_{11}^{(q)}$ for all subvolumes under all loading conditions

$$u_i'^{(q)} = W_{i(00)}^{(q)} + \eta W_{i(10)}^{(q)} + \xi W_{i(01)}^{(q)} + \frac{1}{2}(3\eta^2 - 1)W_{i(20)}^{(q)} + \frac{1}{2}(3\xi^2 - 1)W_{i(02)}^{(q)} \quad (3)$$

The unknown coefficients $W_{i(mn)}^{(q)}$ are ultimately expressed in terms of the surface-averaged displacements.

The local strains are then obtained in terms of the macroscopic and fluctuating strain components upon use of the strain-displacement relations

$$\varepsilon_{ij}^{(q)} = \bar{\varepsilon}_{ij} + \varepsilon_{ij}'^{(q)} = \bar{\varepsilon}_{ij} + \frac{1}{2} \left(\frac{\partial u_i'^{(q)}}{\partial y_j} + \frac{\partial u_j'^{(q)}}{\partial y_i} \right) \quad (4)$$

Subsequently, a local stiffness matrix for the q th subvolume is constructed by relating the surface-averaged fluctuating displacements to the surface-averaged tractions on each face of the subvolume. Toward this end, we express the 15 unknown coefficients $W_{i(mn)}^{(q)}$ in the displacement field representation in terms of the surface-averaged displacements. The definitions of the surface-averaged displacements provide 12 relations between the surface-averaged displacements and the unknown coefficients. These can be compactly expressed in terms of equations relating the first and second order coefficients to the surface-averaged displacements and the zeroth-order coefficients $W_{i(00)}^{(q)}$. The remaining three relations are obtained from the three equilibrium equations satisfied in the large (volume-averaged sense or surface-averaged sense through the Gauss theorem) for each subvolume. The integration of interfacial displacements is done in the $\eta-\xi$ plane, while interfacial tractions are integrated along quadrilateral subvolume faces in the actual microstructure using the coordinate transformation described in the sequel. Following Achenbach [35], the surface-averaged displacements on the p th face of the q th subvolume are defined by

$$\hat{u}_i'^{(1,3)} = \frac{1}{2} \int_{-1}^{+1} u_i'(\eta, \mp 1) d\eta, \quad \hat{u}_i'^{(2,4)} = \frac{1}{2} \int_{-1}^{+1} u_i'(\pm 1, \xi) d\xi \quad (5)$$

which are expressed in terms of the unknown zeroth, first, and second order $W_{i(mn)}^{(q)}$ coefficients upon integration. The superscripts ($p = 1, 2, 3$, and 4) indicate subvolume face number, Fig. 1, omitting for clarity the superscripts (q) which identify a given subvolume.

Similarly, the surface-averaged tractions are defined as follows:

$$\hat{t}_i'^{(1,3)} = \frac{1}{2} \int_{-1}^{+1} t_i(\eta, \mp 1) d\eta, \quad \hat{t}_i'^{(2,4)} = \frac{1}{2} \int_{-1}^{+1} t_i(\pm 1, \xi) d\xi \quad (6)$$

where $t_i'^{(p)} = \sigma_{ji}^{(p)} n_j^{(p)}$ from Cauchy's relations. The stresses associated with each surface are expressed in terms of the corresponding strains through Hooke's law for the q th subvolume

$$\sigma_{ij}^{(q)} = C_{ijkl}^{(q)} (\varepsilon_{kl}^{(q)} - \varepsilon_{kl}^{\text{th}(q)}) \quad (7)$$

where $\varepsilon_{kl}^{\text{th}(q)} = \alpha_{kl}^{(q)} \Delta T$ are thermal strains and $\alpha_{kl}^{(q)}$ are the components of the thermal expansion tensor. The elastic subvolumes may be orthotropic or (transversely) isotropic. The surface-averaged strains on the faces of quadrilateral subvolumes in the actual microstructure needed in the expressions for the surface-averaged tractions are generated using the following relations

between surface-averaged partial derivatives of the displacement field in the two coordinate systems:

$$\begin{bmatrix} \widehat{\frac{\partial u_i'}{\partial y_2}} \\ \widehat{\frac{\partial u_i'}{\partial y_3}} \end{bmatrix}^{(p)} = \hat{\mathbf{J}} \begin{bmatrix} \widehat{\frac{\partial u_i'}{\partial \eta}} \\ \widehat{\frac{\partial u_i'}{\partial \xi}} \end{bmatrix}^{(\hat{p})} \quad \text{where } \hat{\mathbf{J}}^{-1} = \bar{\mathbf{J}} = \frac{1}{4} \int_{-1}^{+1} \int_{-1}^{+1} \mathbf{J} d\eta d\xi \quad (8)$$

where \mathbf{J} is the Jacobian of the transformation. The superscripts p and \hat{p} denote the faces of quadrilateral and reference subvolumes, respectively, with the following correspondence $\hat{p} = 1, 3 \rightarrow \xi = \mp 1$ and $\hat{p} = 2, 4 \rightarrow \eta = \pm 1$. The local stiffness matrix construction is simplified by approximating the relation between surface-averaged displacement gradients on the p th face of the q th subvolume in the reference and actual coordinate systems using volume-averaged Jacobian $\bar{\mathbf{J}}$ in the above equation.

The surface-averaged strains are obtained in terms of the unknown coefficients in the subvolume displacement representation, which are then expressed explicitly in terms of the surface-averaged fluctuating displacement components upon use of the definitions given in Eq. (5) and the application of equilibrium equations in the large (which provide the remaining three equations)

$$\int_{S_q} \boldsymbol{\sigma} \cdot \mathbf{n} dS = \int_{S_q} \mathbf{t} dS = \sum_{p=1}^4 \int_{l_p} \mathbf{t}^{(p)} dl_p = \sum_{p=1}^4 l_p \hat{\mathbf{t}}^{(p)} = 0 \quad (9)$$

This leads to the relationship between the surface-averaged tractions and surface-averaged fluctuating displacements given in terms of the local stiffness matrix $\mathbf{K}^{(q)}$ for the q th subvolume

$$\hat{\mathbf{t}}^{(q)} = \mathbf{K}^{(q)} \hat{\mathbf{u}}'^{(q)} + \mathbf{N}^{(q)} \mathbf{C}^{(q)} (\bar{\varepsilon} - \hat{\varepsilon}^{\text{th}(q)}) \quad (10)$$

where $\hat{\mathbf{t}}^{(q)} = [\hat{\mathbf{t}}^{(1)} \hat{\mathbf{t}}^{(2)} \hat{\mathbf{t}}^{(3)} \hat{\mathbf{t}}^{(4)}]^{(q)\text{T}}$, $\hat{\mathbf{u}}'^{(q)} = [\hat{\mathbf{u}}'^{(1)} \hat{\mathbf{u}}'^{(2)} \hat{\mathbf{u}}'^{(3)} \hat{\mathbf{u}}'^{(4)}]^{(q)\text{T}}$, and $\mathbf{N}^{(q)} = [\mathbf{n}^{(1)} \mathbf{n}^{(2)} \mathbf{n}^{(3)} \mathbf{n}^{(4)}]^{(q)\text{T}}$ contains unit vectors that define the orientation of each of the four subvolume faces. The local stiffness matrix $\mathbf{K}^{(q)}$ is comprised of sixteen submatrices $\mathbf{K}_{ij}^{(q)}$ as shown below, with the elements of each 3×3 submatrix derived in closed form in terms of the subvolume geometry and material properties

$$\mathbf{K}^{(q)} = \begin{bmatrix} \mathbf{K}_{11} & \mathbf{K}_{12} & \mathbf{K}_{13} & \mathbf{K}_{14} \\ \mathbf{K}_{21} & \mathbf{K}_{22} & \mathbf{K}_{23} & \mathbf{K}_{24} \\ \mathbf{K}_{31} & \mathbf{K}_{32} & \mathbf{K}_{33} & \mathbf{K}_{34} \\ \mathbf{K}_{41} & \mathbf{K}_{42} & \mathbf{K}_{43} & \mathbf{K}_{44} \end{bmatrix}^{(q)}$$

2.1.1 Enforcement of Traction and Displacement Continuity at Subvolume Interfaces. The unknown interfacial surface-average displacements are determined by solving a global system of equations generated by first enforcing traction continuity at each interface between two adjacent subvolumes, followed by direct enforcement of displacement continuity. In the present FVDAM version, row- and columnwise unit cell discretization are employed. Hence, proceeding from left to right, row-wise enforcement of traction continuity between adjacent subvolumes takes the form

$$\hat{\mathbf{t}}^{(2,q-1)} + \hat{\mathbf{t}}^{(4,q)} = 0 \quad (11)$$

Similarly, proceeding in the upward direction, columnwise enforcement of traction continuity between adjacent subvolumes takes the form

$$\hat{\mathbf{f}}^{(3,\bar{q}-1)} + \hat{\mathbf{f}}^{(1,\bar{q})} = 0 \quad (12)$$

In the above equations, the superscripts $q-1$, q , and $\bar{q}-1$, \bar{q} are associated with adjacent subvolumes along rows and columns, respectively.

The traction continuity equations are then expressed in terms of surface-averaged displacements, applied macroscopic and thermal strains using the local stiffness matrix relations given by Eq. (10). In the case of intact interfaces, the displacement continuity is satisfied directly by setting equal the interfacial displacements at the common faces of adjacent subvolumes. In the case of interfaces that undergo separation, we introduce displacement discontinuity functions as follows. Proceeding from left to right and then upward, we define

$$\begin{aligned}\hat{\mathbf{u}}'^{(4,q)} - \hat{\mathbf{u}}'^{(2,q-1)} &= \hat{\mathbf{u}}_*^{(4,q)} \\ \hat{\mathbf{u}}'^{(1,\bar{q})} - \hat{\mathbf{u}}'^{(3,\bar{q}-1)} &= \hat{\mathbf{u}}_*^{(1,\bar{q})}\end{aligned}\quad (13)$$

Following Chen and Pindera [24], the interfacial displacements are then expressed in terms of continuous and discontinuous contributions. For the surface-averaged displacements between adjacent subvolumes along the rows, we have

$$\begin{aligned}\hat{\mathbf{u}}'^{(2,q-1)} &= \hat{\mathbf{u}}_o^{(4,q)} - [\mathbf{K}^{*,q}]^{-1} \mathbf{K}_{44}^{(q)} \hat{\mathbf{u}}_*^{(4,q)} \\ \hat{\mathbf{u}}'^{(4,q)} &= \hat{\mathbf{u}}_o^{(4,q)} + [\mathbf{K}^{*,q}]^{-1} \mathbf{K}_{22}^{(q-1)} \hat{\mathbf{u}}_*^{(4,q)}\end{aligned}\quad (14)$$

where $[\mathbf{K}^{*,q}]^{-1} = [\mathbf{K}_{22}^{(q-1)} + \mathbf{K}_{44}^{(q)}]^{-1}$, Fig. 2, and along the columns

$$\begin{aligned}\hat{\mathbf{u}}'^{(3,\bar{q}-1)} &= \hat{\mathbf{u}}_o^{(1,\bar{q})} - [\mathbf{K}^{*,\bar{q}}]^{-1} \mathbf{K}_{11}^{(\bar{q})} \hat{\mathbf{u}}_*^{(1,\bar{q})} \\ \hat{\mathbf{u}}'^{(1,\bar{q})} &= \hat{\mathbf{u}}_o^{(1,\bar{q})} + [\mathbf{K}^{*,\bar{q}}]^{-1} \mathbf{K}_{33}^{(\bar{q}-1)} \hat{\mathbf{u}}_*^{(1,\bar{q})}\end{aligned}\quad (15)$$

where $[\mathbf{K}^{*,\bar{q}}]^{-1} = [\mathbf{K}_{33}^{(\bar{q}-1)} + \mathbf{K}_{11}^{(\bar{q})}]^{-1}$. For intact interfaces, we recover standard interfacial displacement continuity conditions: $\hat{\mathbf{u}}'^{(2,q-1)} = \hat{\mathbf{u}}'^{(4,q)} = \hat{\mathbf{u}}_o^{(4,q)}$ and $\hat{\mathbf{u}}'^{(3,\bar{q}-1)} = \hat{\mathbf{u}}'^{(1,\bar{q})} = \hat{\mathbf{u}}_o^{(1,\bar{q})}$.

Using the above surface-averaged displacement representations in the presence of interfacial separation and assuming isolated interfaces that undergo separation, the traction continuity relations given by Eqs. (11) and (12) become

$$\begin{aligned}\mathbf{K}_{24}^{(q-1)} \hat{\mathbf{u}}_o^{(4,q-1)} + (\mathbf{K}_{22}^{(q-1)} + \mathbf{K}_{44}^{(q)}) \hat{\mathbf{u}}_o^{(4,q)} + \mathbf{K}_{42}^{(q)} \hat{\mathbf{u}}_o^{(4,q+1)} \\ + \mathbf{K}_{21}^{(q-1)} \hat{\mathbf{u}}_o^{(1,\bar{q}-1)} + (\mathbf{K}_{41}^{(q)} + \mathbf{K}_{23}^{(q-1)}) \hat{\mathbf{u}}_o^{(1,\bar{q})} + \mathbf{K}_{43}^{(q)} \hat{\mathbf{u}}_o^{(1,\bar{q}+1)} \\ + (\bar{\mathbf{C}}^{(q-1)} + \bar{\mathbf{C}}^{(q)}) (\bar{\boldsymbol{\epsilon}} - \hat{\boldsymbol{\epsilon}}^{th(q)}) = -\mathbf{L}^{(4,q)} \hat{\mathbf{u}}_*^{(4,q)}\end{aligned}\quad (16)$$

and

$$\begin{aligned}\mathbf{K}_{31}^{(\bar{q}-1)} \hat{\mathbf{u}}_o^{(1,\bar{q}-1)} + (\mathbf{K}_{33}^{(\bar{q}-1)} + \mathbf{K}_{11}^{(\bar{q})}) \hat{\mathbf{u}}_o^{(1,\bar{q})} + \mathbf{K}_{13}^{(\bar{q})} \hat{\mathbf{u}}_o^{(1,\bar{q}+1)} \\ + \mathbf{K}_{34}^{(\bar{q}-1)} \hat{\mathbf{u}}_o^{(4,q-1)} + (\mathbf{K}_{32}^{(\bar{q}-1)} + \mathbf{K}_{14}^{(\bar{q})}) \hat{\mathbf{u}}_o^{(4,q)} + \mathbf{K}_{12}^{(\bar{q})} \hat{\mathbf{u}}_o^{(4,q+1)} \\ + (\bar{\mathbf{C}}^{(\bar{q}-1)} + \bar{\mathbf{C}}^{(\bar{q})}) (\bar{\boldsymbol{\epsilon}} - \hat{\boldsymbol{\epsilon}}^{th(q)}) = -\mathbf{L}^{(1,\bar{q})} \hat{\mathbf{u}}_*^{(1,\bar{q})}\end{aligned}\quad (17)$$

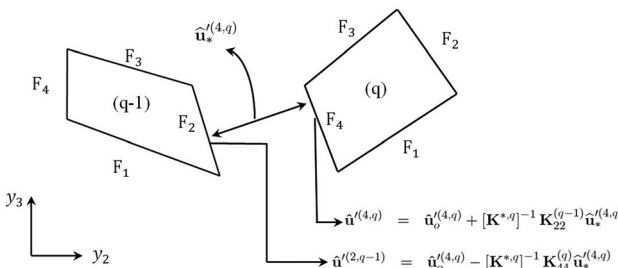


Fig. 2 Interfacial discontinuity between two adjacent subvolumes

where

$$\begin{aligned}\mathbf{L}^{(4,q)} &= (\mathbf{K}_{44}^{(q)} [\mathbf{K}^{*,q}]^{-1} \mathbf{K}_{22}^{(q-1)} - \mathbf{K}_{22}^{(q-1)} [\mathbf{K}^{*,q}]^{-1} \mathbf{K}_{44}^{(q)}) \\ \mathbf{L}^{(1,\bar{q})} &= (\mathbf{K}_{11}^{(\bar{q})} [\mathbf{K}^{*,\bar{q}}]^{-1} \mathbf{K}_{33}^{(\bar{q}-1)} - \mathbf{K}_{33}^{(\bar{q}-1)} [\mathbf{K}^{*,\bar{q}}]^{-1} \mathbf{K}_{11}^{(\bar{q})})\end{aligned}$$

In the presence of additional separations along the remaining interfaces of the adjacent subvolumes ($q-1$, q) and ($\bar{q}-1$, \bar{q}) the above equations would be modified accordingly.

2.2 Primary and Auxiliary Global Systems of Equations.

Imposition of interfacial traction and displacement continuity conditions at internal subvolume faces, together with periodicity conditions at external subvolume faces and elimination of rigid body motion, cf. Bansal and Pindera [30], produces the global system of equations containing common surface-averaged fluctuating displacements and displacement discontinuities that symbolically takes the form

$$\mathbb{K} \hat{\mathbf{U}}'_o = \Delta \mathbf{C} \bar{\boldsymbol{\epsilon}} + \Delta \Gamma \Delta T - \mathbb{L} \hat{\mathbf{U}}'_* \quad (18)$$

In the above, \mathbb{K} is the global stiffness matrix containing information on subvolume geometry and material assignment, the matrix $\Delta \mathbf{C}$ is comprised of differences in material stiffness matrices of adjacent subvolumes, \mathbb{L} is the matrix that represents contributions from damaged or cracked interfaces, and $\bar{\boldsymbol{\epsilon}}$ is the applied (specified) homogenized strain that represents loading. This is the primary system of equations that is used to express the continuous surface-averaged fluctuating interfacial displacements $\hat{\mathbf{U}}'_o$ in terms of the corresponding displacement discontinuities $\hat{\mathbf{U}}'_*$. The additional or auxiliary equations necessary for the determination of the displacement discontinuities come from the traction conditions applied to the damaged interfaces described next.

The interfacial tractions are related to the fluctuating surface-averaged common displacements and the corresponding displacement discontinuities in the presence of interfacial damage via the local stiffness matrix expression given in Eq. (10). In the latter case, tractions may be specified directly, e.g., using traction-free crack-face condition or via a chosen traction-interfacial separation relation. In the presence of multiple interfaces undergoing damage, the local stiffness matrix relationship for a particular interface involves displacement discontinuities associated with the faces of the particular subvolume as well as displacement discontinuities associated with other interfaces. This coupling comes through the adjacent continuous surface-averaged interfacial displacements obtained from the solution of the primary system of equations. The auxiliary equations for the tractions along the interfaces undergoing damage may be symbolically expressed as follows:

$$\mathbf{T} = \mathbf{K}_* \hat{\mathbf{U}}'_* + \mathbf{K}_o \hat{\mathbf{U}}'_o + \mathbb{C} \bar{\boldsymbol{\epsilon}} + \Gamma \Delta T \quad (19)$$

where the matrix \mathbf{K}_* contains the elements associated with displacement discontinuities, which are products of the local stiffness matrices $\mathbf{K}^{(q)}$ and elements of the matrices appearing in Eqs. (14) and (15), \mathbf{K}_o contains the local stiffness matrices associated with the undamaged interfaces, and $\mathbb{C} \bar{\boldsymbol{\epsilon}}$ and $\Gamma \Delta T$ are the assembled loading vectors. From the primary system of equations, we then obtain the continuous fluctuating surface-averaged interfacial displacements in terms of displacement discontinuities

$$\hat{\mathbf{U}}'_o = \mathbb{K}^{-1} (\Delta \mathbf{C} \bar{\boldsymbol{\epsilon}} + \Delta \Gamma \Delta T - \mathbb{L} \hat{\mathbf{U}}'_*) \quad (20)$$

Substituting the expression for $\hat{\mathbf{U}}'_o$ into the auxiliary system of equations, we finally obtain the auxiliary system of equations that relates the tractions of damaged interfaces to the corresponding displacement discontinuities and the applied loading,

$$\mathbf{T}(\hat{\mathbf{U}}'_*) = (\mathbf{K}^* - \mathbf{K}_o \mathbb{K}^{-1} \mathbb{L}) \hat{\mathbf{U}}'_* + \mathbf{K}_o \mathbb{K}^{-1} \Delta \mathbf{C} \bar{\boldsymbol{\varepsilon}} + \mathbf{K}_o \mathbb{K}^{-1} \Delta \boldsymbol{\Gamma} \Delta T + \mathbb{C} \bar{\boldsymbol{\varepsilon}} + \boldsymbol{\Gamma} \Delta T \quad (21)$$

The tractions appearing on the left hand side of the auxiliary system of equations may be specified directly or through a chosen traction-displacement discontinuity relation $\mathbf{T}(\hat{\mathbf{U}}'_*)$. In the case of a nonlinear traction-displacement discontinuity relation, an incremental and iterative (Newton–Raphson) procedure is applied to solve the auxiliary system of equations.

2.3 Cohesive Zone Model Implementation. Herein, we incorporate the coupled bilinear traction-separation relation frequently employed in finite-element CZM-based damage evolution studies, cf. Geubelle and Baylor [36], Chandra et al. [37], Matous and Geubelle [38], and Song et al. [39]. The nondimensional effective separation displacement defined by

$$\lambda_e = \sqrt{\left(\frac{\delta_n}{\Delta_n^c}\right)^2 + \left(\frac{\delta_t}{\Delta_t^c}\right)^2} \quad (22)$$

is employed to couple the normal traction-displacement discontinuity and shear traction-displacement discontinuity relations. In the above definition, δ_n and δ_t are the normal and tangential displacement discontinuities, and Δ_n^c and Δ_t^c are the corresponding critical values at complete separation. Following common practice, we set the critical values equal, $\Delta_n^c = \Delta_t^c = \Delta^c$. The maximum nondimensional displacement λ_{\max} , which corresponds to the maximum tractions, is incorporated to adjust the elastic stiffness by adjusting the prepeak slope of the traction-separation relation. With the above defined quantities, the bilinear interfacial separation relation takes the following forms for the respective loading cases when the interface is under tension:

For $\delta_n > 0$ and $\lambda_e < \lambda_{\max}$

$$t_n = \sigma_{\max} \frac{1}{\lambda_{\max}} \left(\frac{\delta_n}{\Delta^c} \right), \quad t_t = \sigma_{\max} \frac{1}{\lambda_{\max}} \left(\frac{\delta_t}{\Delta^c} \right) \quad (23)$$

For $\delta_n > 0$ and $\lambda_e > \lambda_{\max}$

$$t_n = \sigma_{\max} \frac{1 - \lambda_e}{1 - \lambda_{\max}} \frac{1}{\lambda_e} \left(\frac{\delta_n}{\Delta^c} \right), \quad t_t = \sigma_{\max} \frac{1 - \lambda_e}{1 - \lambda_{\max}} \frac{1}{\lambda_e} \left(\frac{\delta_t}{\Delta^c} \right) \quad (24)$$

When the interface is under compression, $\delta_n = 0$ and only the shear traction relations hold in the above.

In order to implement an iterative Newton–Raphson technique in the solution of Eq. (21), the Jacobian of the stiffness matrix obtained from the gradient form of the traction-interfacial separation relations is required

$$\begin{bmatrix} dt_n \\ dt_t \end{bmatrix} = \begin{bmatrix} \frac{\partial t_n}{\partial \delta_n} & \frac{\partial t_n}{\partial \delta_t} \\ \frac{\partial t_t}{\partial \delta_n} & \frac{\partial t_t}{\partial \delta_t} \end{bmatrix} \begin{bmatrix} d\delta_n \\ d\delta_t \end{bmatrix} = \begin{bmatrix} C_{nn} & C_{nt} \\ C_{tn} & C_{tt} \end{bmatrix} \begin{bmatrix} d\delta_n \\ d\delta_t \end{bmatrix} \quad (25)$$

For $\lambda_e < \lambda_{\max}$

$$\begin{aligned} C_{nn} &= \frac{\partial t_n}{\partial \delta_n} = \frac{\sigma_{\max}}{\lambda_{\max} \Delta^c} \\ C_{nt} &= C_{tn} = 0 \\ C_{tt} &= \frac{\partial t_t}{\partial \delta_t} = \frac{\sigma_{\max}}{\lambda_{\max} \Delta^c} \end{aligned} \quad (26)$$

For $\lambda_e > \lambda_{\max}$

$$\begin{aligned} C_{nn} &= \frac{\partial t_n}{\partial \delta_n} = \frac{\sigma_{\max}}{(1 - \lambda_{\max}) \Delta^c} \left(\frac{1}{\lambda_e} - \frac{(\delta_n)^2}{(\Delta^c)^2} \frac{1}{\lambda_e^3} - 1 \right) \\ C_{nt} &= \frac{\partial t_n}{\partial \delta_t} = -\frac{\sigma_{\max}}{(1 - \lambda_{\max}) (\Delta^c)^3} \frac{\delta_n \delta_t}{\lambda_e^3} \frac{1}{\lambda_e^3} \\ C_{tn} &= \frac{\partial t_t}{\partial \delta_n} = -\frac{\sigma_{\max}}{(1 - \lambda_{\max}) (\Delta^c)^3} \frac{\delta_t \delta_n}{\lambda_e^3} \frac{1}{\lambda_e^3} \\ C_{tt} &= \frac{\partial t_t}{\partial \delta_t} = \frac{\sigma_{\max}}{(1 - \lambda_{\max}) \Delta^c} \left(\frac{1}{\lambda_e} - \frac{(\delta_t)^2}{(\Delta^c)^2} \frac{1}{\lambda_e^3} - 1 \right) \end{aligned} \quad (27)$$

Figure 3 illustrates graphically the coupled normal and tangential interfacial separation laws and the resulting interaction effects. The coupling between the normal and tangential modes may be eliminated by eliminating coupling in the expression for the nondimensionalized effective separation displacement. In this case, strictly bilinear traction-interfacial separation relations for each mode are obtained, which are also included in Fig. 3. These correspond to the planes $\delta_t = 0$ and $\delta_n = 0$ in the normal and tangential separation laws, respectively.

The interfacial separation laws are given in terms of normal and tangential displacement discontinuities, whereas the displacement discontinuities defined within the FVDAM framework, Eqs. (14) and (15), are referred to the Cartesian coordinate system associated with the unit cell. Hence, in order to implement the above separation laws into the FVDAM framework, the traction and displacement discontinuities appearing in the auxiliary global equations, Eq. (21), are transformed to local coordinate systems that are normal and tangential to the subvolume faces undergoing separation. When the normal traction is compressive for the particular interface, the corresponding equation in the transformed system of auxiliary equations is simply eliminated and the standard traction and displacement continuity conditions, expressed through the common surface-averaged displacements appearing in the primary system of equations, suffice. This straightforward approach of implementing CZM into our finite-volume framework, enabled by partitioning the surface-averaged interfacial displacements using Eqs. (14) and (15), contrasts with the corresponding finite-element based implementation where large interfacial stiffness is employed in the interfacial traction-separation law in compression, potentially leading to material interpenetration.

2.4 Homogenization. Solution of the auxiliary system of equations for the surface-averaged displacement discontinuities $\hat{\mathbf{U}}'_*$, followed by the determination of the continuous surface-averaged fluctuating displacements $\hat{\mathbf{U}}'_o$, enables determination of the localization relations for the q th subvolume

$$\bar{\boldsymbol{\varepsilon}}^{(q)} = \mathbb{A}^{(q)} \bar{\boldsymbol{\varepsilon}} + \mathbb{D}^{(q)} \quad (28)$$

where $\mathbb{A}^{(q)}$ are Hill's strain concentration matrices [40]. Application of one nonzero macroscopic strain component in the absence of damage determines one column vector of $\mathbb{A}^{(q)}$, which is done just once. On the other hand, the vector $\mathbb{D}^{(q)}$, which contains thermal and displacement discontinuity contributions to the q th subvolume average strain, is obtained at each increment of the applied macroscopic strains $\bar{\boldsymbol{\varepsilon}}$ upon solution of the unit cell boundary-value problem, which generates $\bar{\boldsymbol{\varepsilon}}^{(q)}$. Hence, $\mathbb{D}^{(q)} = \bar{\boldsymbol{\varepsilon}}^{(q)} - \mathbb{A}^{(q)} \bar{\boldsymbol{\varepsilon}}$. Use of localization relations in the average composite stress definition, in conjunction with the volume-averaged stress-strain relations for each subvolume, yields the homogenized or macroscopic constitutive equation for a multiphase composite in the presence of evolving interfacial damage

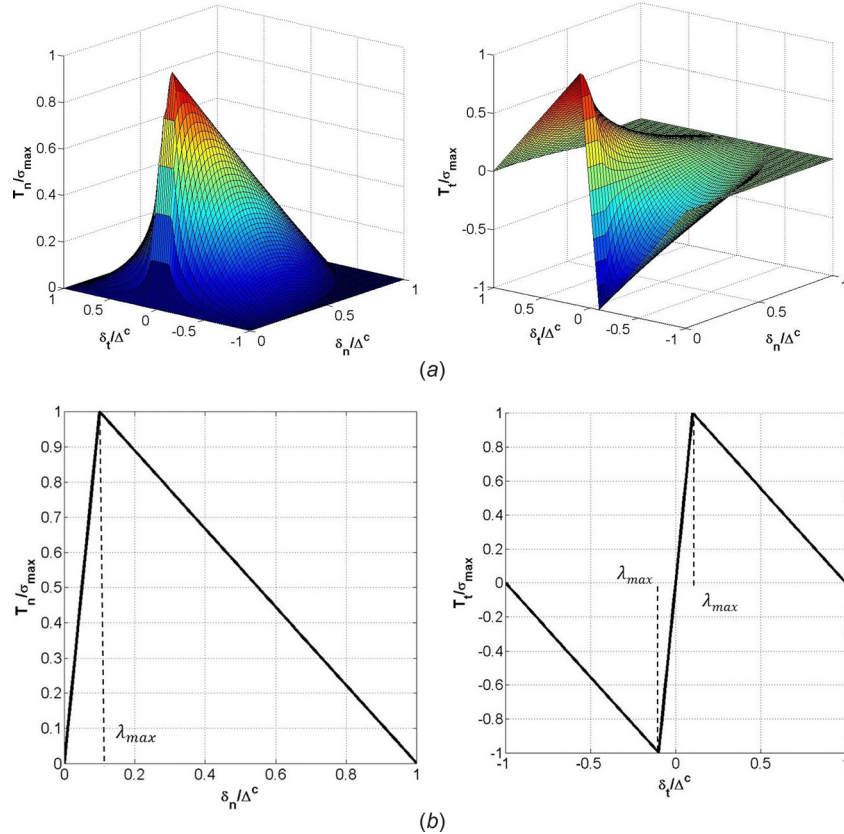


Fig. 3 Traction-interfacial separation relations for the CZM in normal (left column) and tangential (right column) directions to the interface: graphical representations of (a) coupled and (b) uncoupled relations

$$\bar{\sigma} = \frac{1}{V} \int_V \sigma(x) dV = \sum_{q=1}^{N_q} v_{(q)} \bar{\sigma}^{(q)} = \mathbf{C}^* [\bar{\epsilon} - (\bar{\epsilon}^{\text{th}} + \bar{\epsilon}^{\text{d}})] \quad (29)$$

where $v_{(q)} = V^{(q)}/V$ is the volume fraction of the q th subvolume. The homogenized stiffness matrix \mathbf{C}^* and the thermal and damage strains are given in terms of the subvolume geometry, material properties, elastic concentration matrices, and their thermodamage counterparts

$$\begin{aligned} \mathbf{C}^* &= \sum_{q=1}^{N_q} v_{(q)} \mathbf{C}^{(q)} \mathbb{A}^{(q)}, \\ \bar{\epsilon}^{\text{th}} + \bar{\epsilon}^{\text{d}} &= -\frac{[\mathbf{C}^*]^{-1}}{V} \sum_{q=1}^{N_q} v_{(q)} [\mathbf{C}^{(q)} \mathbb{D}^{(q)} - \mathbf{F}^{(q)} \Delta T] \end{aligned} \quad (30)$$

The implementation of the CZM is presently limited to loading by combined homogenized strains in the plane perpendicular to the continuous reinforcement direction, i.e., the $x_2 - x_3$ plane, by a combination of the inplane homogenized strains $\bar{\epsilon}_{22}$, $\bar{\epsilon}_{23}$, or $\bar{\epsilon}_{33}$ under the generalized plane strain constraint $\bar{\epsilon}_{11}$. This capability may be used to generate the homogenized response $\bar{\sigma}_{22} - \bar{\sigma}_{23}$, $\bar{\sigma}_{23} - \bar{\sigma}_{33}$, or $\bar{\sigma}_{33} - \bar{\sigma}_{23}$ under unidirectional loading conditions, along with the corresponding homogenized moduli C_{22}^* , C_{23}^* , C_{33}^* , or C_{44}^* . As observed in Eqs. (18)–(21), the solution of the unit cell boundary-value problem is obtained for any combination of specified macroscopic strains $\bar{\epsilon}$. In order to simulate loading by specified stress components, the strain components are adjusted accordingly using the homogenized constitutive equation $\bar{\sigma} = \mathbf{C}^*([\bar{\epsilon} - (\bar{\epsilon}^{\text{th}} + \bar{\epsilon}^{\text{d}})])$. In the absence of damage and thermal loads, constant strain ratios that correspond to fixed stress ratios are obtained in terms of the homogenized moduli \mathbf{C}^* . In the

presence of damage and thermal loads, the incremental version of the homogenized constitutive equations

$$d\bar{\sigma} = \mathbf{C}^*(d\bar{\epsilon} - d\bar{\epsilon}^{\text{d}} - d\bar{\epsilon}^{\text{th}}) \quad (31)$$

is employed, and strain increment ratios are adjusted iteratively at each load increment to generate the desired load path specified in terms of macroscopic stresses.

The above CZM-based homogenization framework may be checked for consistency by comparing the applied macroscopic strains $\bar{\epsilon}$ with the homogenized strains obtained from the solution of the unit cell boundary-value problem at each load increment. Specifically, the average strain obtained from the unit cell surface displacements

$$\bar{\epsilon}_{ij} = \frac{1}{V} \int_S \frac{1}{2} (u_i n_j + u_j n_i) dS \quad (32)$$

may be expressed in terms of the volume average subvolume contributions through the use of Gauss theorem and the contributions due to the displacement discontinuities, yielding

$$\begin{aligned} \bar{\epsilon}_{ij} &= \frac{1}{V} \int_V \epsilon_{ij}(\mathbf{x}) dV - \frac{1}{2V} \int_{S_d} (\delta u_i n_j + \delta u_j n_i) dS \\ &= \sum_{q=1}^{N_q} v_{(q)} \bar{\epsilon}_{ij}^{(q)} - \frac{1}{2V} \sum_{q=1}^{N_q} l_d^{(q)} (\delta \hat{u}_i^{(q)} n_j + \delta \hat{u}_j^{(q)} n_i) \end{aligned} \quad (33)$$

where N_q^* is the number of damaged interfaces, $l_d^{(q)}$ is the length of the damaged interface, and $\delta \hat{u}_i^{(q)}$ are the surface-averaged displacement discontinuities. This formula will be employed

Table 1 Elastic parameters for the modified Eshelby problem

Material	E (GPa)	ν	$k_r^* = k_\theta^*$ (MPa/length)
Inclusion	100	0.35	—
Matrix	400	0.25	—
Interface	—	—	3.0×10^6

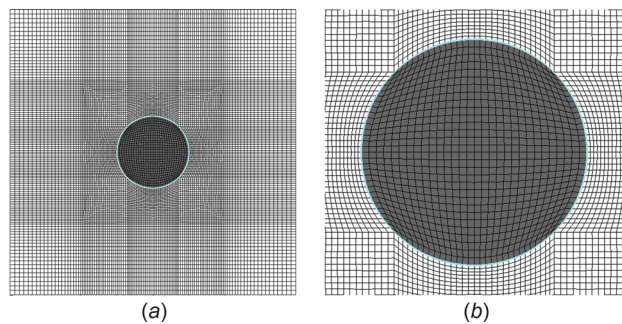


Fig. 4 Unit cell geometry containing 0.05 fiber volume fraction (left) and a detailed close-up (right) used for comparison with the Eshelby solution for an inclusion with a linear interface in an infinite matrix

to verify the correctness of the implemented CZM and the accuracy of the CZM-based solution for the investigated unit cell problems.

3 Verification

The implemented CZM capability is first validated in the linear region by comparison with an exact elasticity solution for an inclusion surrounded by a linear interface of zero thickness that obeys the same constitutive law as CZM before the onset of unloading. The inclusion is embedded in an infinite matrix and subjected to uniform far-field loading by σ_{22}^∞ . This is the classical Eshelby problem [41], with a linearly elastic flexible interface whose solution can be readily obtained by specializing the available solutions in cylindrical coordinates, cf. Drago and Pindera [42]. In particular, the displacement field in the inclusion and the matrix under plain strain conditions that satisfies the Navier's equations and far-field loading condition reads

$$u_r^f(r, \theta) = A_{10}^f r - [2/3\nu_f/(3-2\nu_f)A_{12}^f r^3 + A_{22}^f r] \cos 2\theta \quad (34)$$

$$u_\theta^f(r, \theta) = (A_{12}^f r^3/3 + A_{22}^f r) \sin 2\theta$$

and

$$u_r^m(r, \theta) = A_{10}^m r + A_{20}^m/r + (-A_{22}^m r - A_{32}^m r^{-3}/3 + 2(1-\nu_m)/(1-2\nu_m)A_{42}^m r^{-1}) \cos 2\theta \quad (35)$$

$$u_\theta^m(r, \theta) = (A_{22}^m r - A_{32}^m r^{-3}/3 - A_{42}^m r^{-1}) \sin 2\theta$$

The unknown coefficients A_{10}^m and A_{22}^m are obtained from the far-field loading condition

$$\sigma_{rr}^m(r \rightarrow \infty, \theta) = 1/2\sigma_{22}^\infty(1 - \cos 2\theta) \quad (36)$$

and the remaining six unknown coefficients are determined from displacement discontinuity conditions at the fiber/matrix interface $r=a$

$$u_r^m(a, \theta) - u_r^f(a, \theta) = u_r^* \quad \text{and} \quad u_\theta^m(a, \theta) - u_\theta^f(a, \theta) = u_\theta^* \quad (37)$$

where the interfacial constitutive relations are

$$\sigma_{rr}^{\text{int}} = k_r^* u_r^* \quad \text{and} \quad \sigma_{\theta\theta}^{\text{int}} = k_\theta^* u_\theta^* \quad (38)$$

and interfacial traction continuity conditions

$$\sigma_{rr}^f(a, \theta) = \sigma_{rr}^m(a, \theta) \quad \text{and} \quad \sigma_{r\theta}^f(a, \theta) = \sigma_{r\theta}^m(a, \theta) \quad (39)$$

For comparison purposes, we employ the uncoupled CZM separation law with $k_r^* = k_\theta^*$ and choose fiber and matrix material parameters given in Table 1, which do not produce cohesive zone interpenetration due to the applied horizontal loading. A different solution strategy would be required if this were not the case. The unit cell constructed for FVDAM computations for comparison with the modified Eshelby solution is shown in Fig. 4, together with a close-up of the interfacial region. The fiber radius is one, producing volume fraction for this unit cell of 0.05, and the discretization employed is 120×120 subvolumes. Figure 5 illustrates comparison of the interfacial displacement discontinuities along radial and tangential directions under loading by $\sigma_{22}^\infty = 1$ MPa, and plane strain condition $\bar{\epsilon}_{11} = 0$ along the fiber direction. As observed, the FVDAM results coincide with the modified Eshelby solution nearly everywhere around the entire fiber/matrix interface both in the radial and tangential directions.

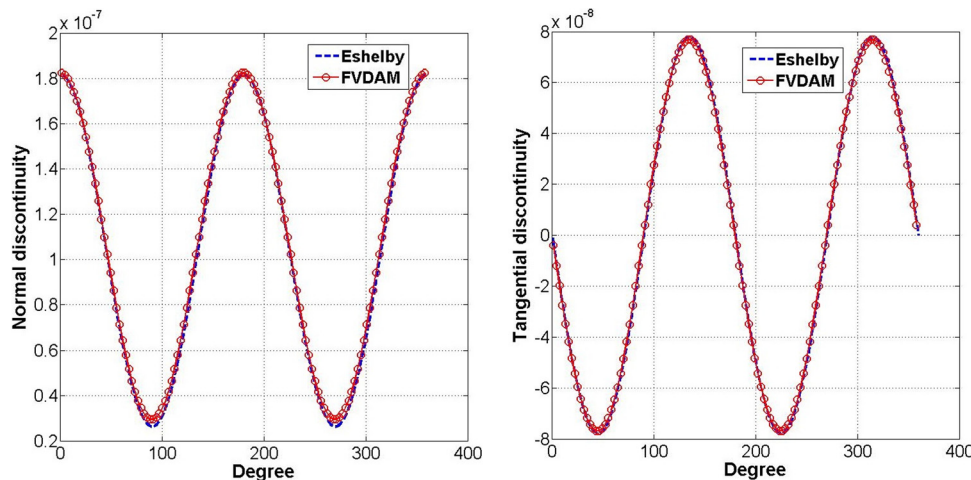


Fig. 5 Comparison of radial and tangential displacement discontinuities around the fiber/matrix interface obtained from modified Eshelby and dilute FVDAM solutions

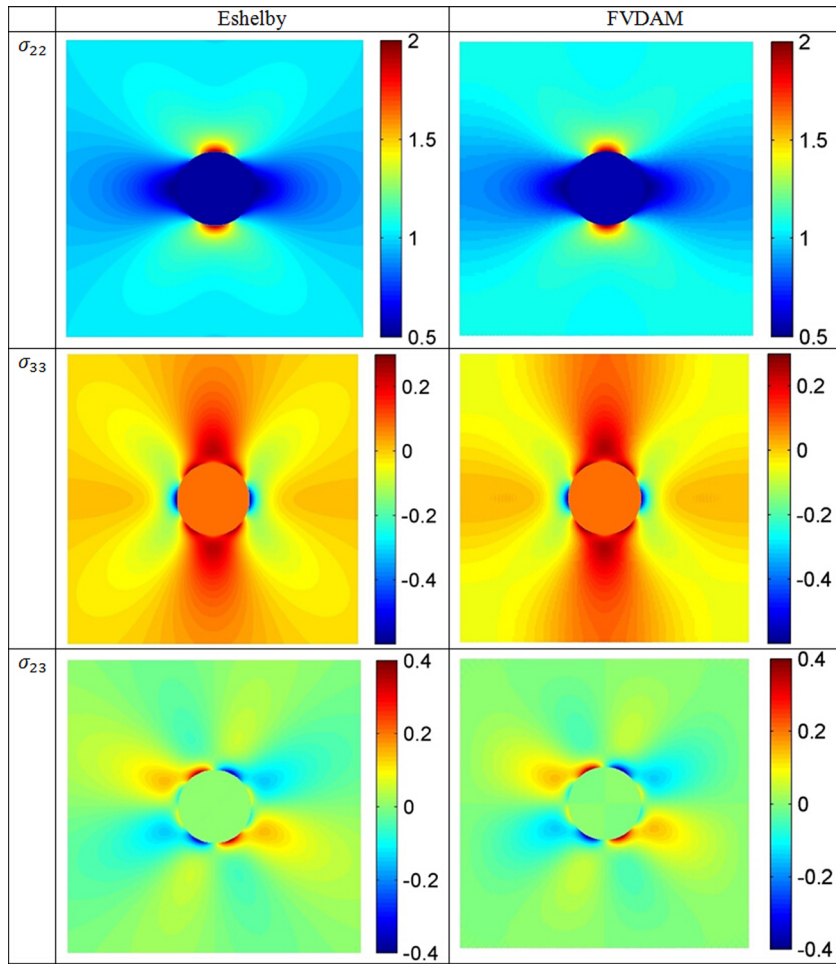


Fig. 6 Comparison of normal and tangential stress fields in the region occupied by the unit cell obtained from modified Eshelby and dilute FVDAM solutions based on the interfacial properties in Table 1

Similar observation holds for the normal and tangential traction distributions (not shown). The corresponding full-field stress distributions in Cartesian coordinates, $\sigma_{22}(y_2, y_3)$, $\sigma_{23}(y_2, y_3)$, and $\sigma_{33}(y_2, y_3)$, are given in Fig. 6 and demonstrate the accuracy of the FVDAM predictive capability with the newly incorporated CZM in the linearly elastic range. We note that the $\sigma_{22}(a, \pi/2)$ stress concentration is substantially less than three because the fiber/matrix Young's modulus mismatch is just 1/4 for this case and $k_r^* = 3 \times 10^6$ MPa/unit length. To demonstrate that the FVDAM theory with the implemented CZM can reproduce the well-known Kirsch solution, which produces the stress concentration factor of 3 at the apex of the hole under horizontal loading, we can either reduce the interfacial stiffness to a negligible level or reduce the fiber Young's modulus without changing the interfacial stiffness such that the fiber approximates a circular hole. Both approaches were taken. Figure 7 compares the normal and tangential stress distributions for the case when the interfacial stiffness has been degraded to a small number, namely, $k_r^* = 3$ MPa/unit length. As observed, the stress magnification of three is obtained as in the Kirsch problem. The same distributions are obtained when the inclusion properties are reduced to a very small number and the interfacial stiffness is kept at $k_r^* = 3 \times 10^6$ MPa/unit length.

4 Fiber/Matrix Debonding in SiC/Ti Composites Revisited

To demonstrate the capability of the implemented CZM within the FVDAM framework in simulating progressive interfacial

damage evolution leading to phase separation in heterogeneous materials, we revisit the classic SiC/Ti debonding problem. Unidirectionally reinforced SiC/Ti composites were first proposed in the 1980s to increase the operating temperature of aircraft engine turbine blades. However, the high consolidation temperature of the SiC/Ti material system produced a chemical reaction at the fiber/matrix interface, which resulted in substantially degraded chemical bond, leading to premature fiber/matrix interfacial debonding at low transverse normal stresses. Hence, this system is a good candidate to validate the predictive capability of the CZM-based FVDAM theory relative to the available experimental data reported by Johnson et al. [43].

The unit cell representative the unidirectional SiC/Ti composite in the cross section normal to the fiber direction and its discretization into 52×52 subvolumes is similar to that shown in Fig. 4(b) for the Eshelby problem in the vicinity of the cylindrical inclusion, with the highlighted cohesive zone around the entire fiber. The SiC fiber volume fraction is 0.325, the diameter of the fiber is $142 \mu\text{m}$, and the unit cell dimensions are $221 \times 221 \mu\text{m}$. The elastic moduli and thermal expansion coefficients of the phases are given in Table 2. The yield stress of the titanium matrix included in the table was used to ensure that the simulated response remained elastic, as plastic effects were not included in the CZM implementation in the present version. Given that the interfacial elastic parameters are not known for the SiC/Ti system, the value of the initial stiffness was chosen such that the initial response of the unit cell coincided with the experimentally measured transverse response of the unidirectional SiC/Ti composite. The value

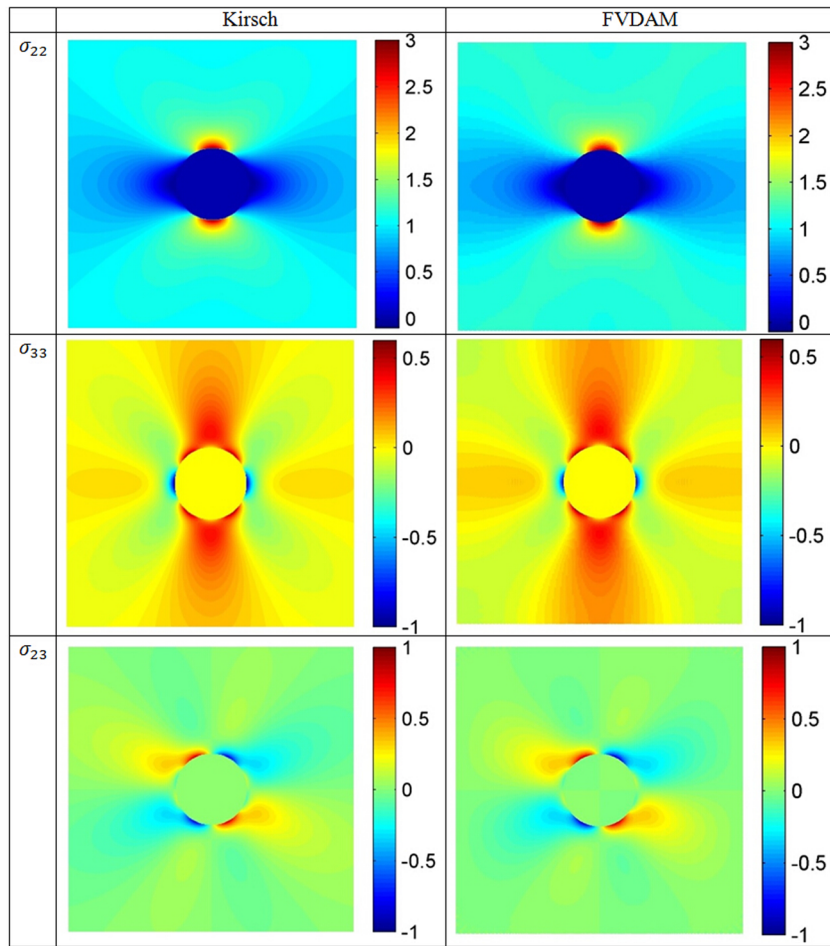


Fig. 7 Comparison of normal and tangential stress fields in the region occupied by the unit cell obtained from modified Eshelby and dilute FVDAM solutions with the interfacial properties set to simulate the Kirsch solution

Table 2 Thermoelastic properties of the SiC fibers and Ti matrix

Material	E (GPa)	ν	α ($\mu/\text{ }^{\circ}\text{C}$)	σ_y (MPa)
SCS ₆	400	0.25	4.86	—
Ti-15	92.38	0.35	9.72	689.5

of the final separation distance was based on the maximum interfacial strength of 138 MPa (which coincides with the knee of the homogenized stress-strain curve) and the ratio between the elastic limit of initial separation and final separation of ten suggested by Geubelle and Baylor [36]. Hence, the only parameter that was varied, in order to determine the optimum value that produced the best correlation with experimental data during the interfacial degradation stage of the response, was interfacial strength, Table 3.

In order to model residual stresses after consolidation, the unidirectional SiC/Ti composite was first subjected to a temperature cooldown, which was followed by pure transverse loading. Following Johnson et al. [43], temperature cooldown of $\Delta T = -555\text{ }^{\circ}\text{C}$ was employed to simulate fabrication-induced residual stresses. This was based on the observation that any stresses that may develop during the fabrication process at the actual consolidation temperature greater than one half of the melting point of the matrix would be relieved due to creep [44]. The inclusion of residual stresses is critically important in correctly capturing the fiber/matrix interfacial separation mechanism owing to the high compressive radial stress at the interface that must be first

Table 3 Interfacial strength parameters for the SiC/Ti composite. Note: $k_n^o = \sigma_{\max}/\Delta_n^o$.

$\sigma_{\max} = \tau_{\max}$ (MPa)	$k_n^o = k_t^o$ (MPa/ μm)	$\Delta_n^o = \Delta_t^o$ (μm)	$\Delta_n^c = \Delta_t^c$ (μm)
138	3000	0.0460	0.46
70	3000	0.0233	0.46
50	3000	0.0167	0.46

overcome by the applied load. Two cases were then considered for comparison with the experimental data. First, the breaking of the chemical bond leading to fiber/matrix interfacial separation was modeled by the CZM during initial transverse loading immediately following fabrication cooldown in the absence of prior mechanical preload. Subsequently, the composite was subjected to transverse loading in the presence of residual stresses but with the chemical bond assumed to be destroyed over a certain arc length of the fiber/matrix interface by the initial preload. In this case, the interfacial separation occurred when the residual radial stress at the fiber/matrix interface was overcome by the applied transverse load. The individual results are presented in the sequel.

4.1 Progressive Interfacial Degradation After Fabrication Cooldown. The response of the SiC/Ti composite under transverse loading is simulated immediately after the fabrication cooldown when the fiber/matrix interface is presumed intact. In this case, the interface is assumed to be capable of supporting load in both normal and tangential directions. To demonstrate the

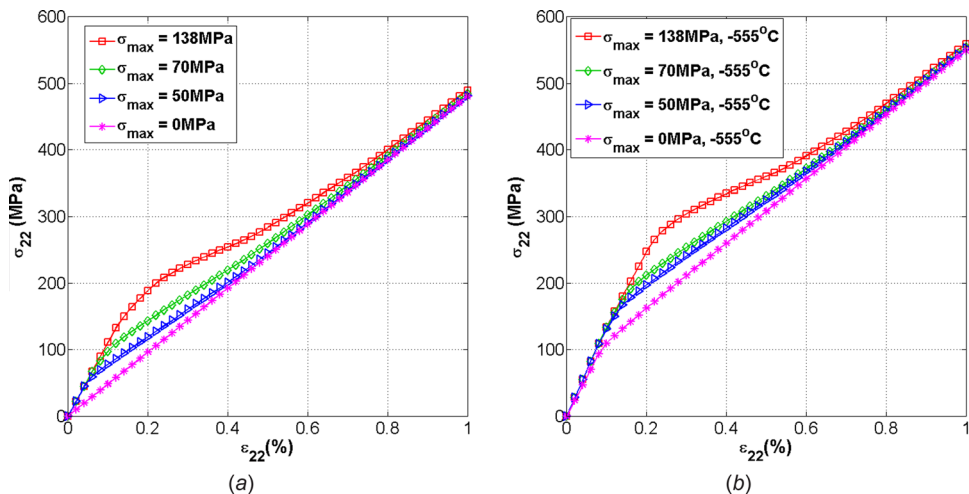


Fig. 8 Initial transverse response of the unidirectional SiC/Ti composite with different interfacial strengths, illustrating the effect of fabrication-induced residual stresses

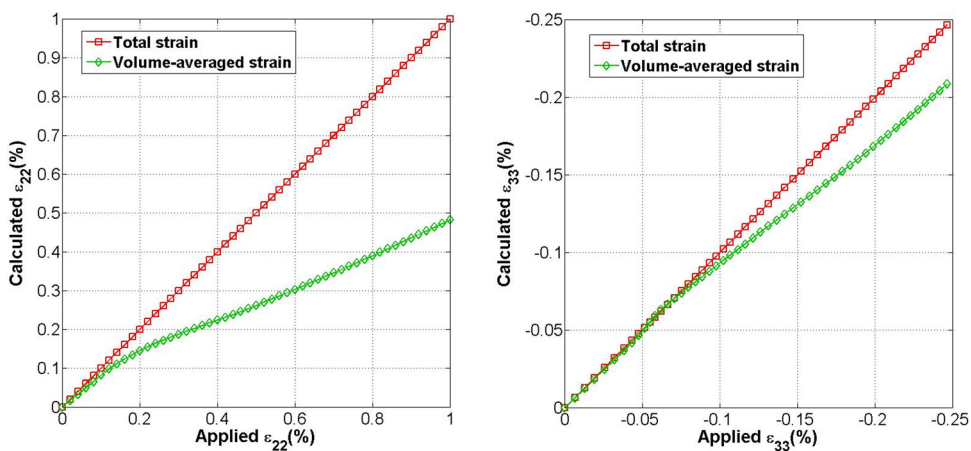


Fig. 9 Comparison of the applied (vertical axis) and calculated (horizontal axis) homogenized strains based on Eq. (33), demonstrating consistency and accuracy of the implemented solution technique for the nonlinear response of the unit cell based on the implemented CZM, and importance of the contributions of the interfacial displacement discontinuities toward total homogenized strains

importance of residual stresses, Fig. 8 presents comparison of homogenized transverse responses generated using temperature changes of $\Delta T = 0^\circ\text{C}$ and $\Delta T = -555^\circ\text{C}$ for interfacial strengths ranging from 138 MPa to 0 MPa. For this comparison, the uncoupled interfacial separation law was employed. The asymptotic responses, which converge to the same limiting behavior regardless of the interfacial strength magnitude, which also depend on the cooldown temperature, provide additional validation of the implemented CZM in the nonlinear region when the interface undergoes degradation. The same asymptotic response is expected upon complete separation of the fiber/matrix interface along the largest possible arc length before its arrest regardless of the interfacial strength magnitude, as was also observed by Raghavan and Ghosh [45] in the absence of residual stresses. The presence of residual stresses shifts the asymptotic homogenized response upward as additional load is required to overcome the radial compressive stress at the fiber/matrix interface before separation initiates. Figure 9 provides a consistency and an accuracy check of the unit cell solution procedure in the presence of evolving damage through comparison of the applied homogenized strains that appear as loading parameters in the solution of the unit cell problem, Eqs. (18) and (21), and the corresponding

homogenized strains calculated from the volume-averaged subvolume local strains and surface-averaged displacement discontinuities, Eq. (33). Included in the figure is the comparison between the applied homogenized strains and the volume-averaged strains alone in order to demonstrate the contribution of the surface-averaged displacement discontinuities. The above results, generated using $\Delta T = 0^\circ\text{C}$ and the interfacial strength of 138 MPa, provide additional confidence in the simulations that follow.

Comparison of the simulated results after the $\Delta T = -555^\circ\text{C}$ cooldown shown in Fig. 8(b) with experimental data of Johnson et al. [43] reveals that the best correlation is obtained with the interfacial strength of 50 MPa. This comparison is illustrated in Fig. 10, which also includes the corresponding comparison based on the coupled separation law with the interfacial strengths of 50 MPa and 70 MPa. As anticipated from the graphical illustration of the interfacial separation laws shown in Fig. 3, the use of the coupled separation law produces a softer response for the same interfacial strength of 50 MPa, requiring a higher interfacial strength to attain comparable accuracy, namely, 70 MPa in the present case. In subsequent presentation of the simulation results, we will employ the uncoupled separation law as it appears to yield somewhat better results. This difference, however, may be due to

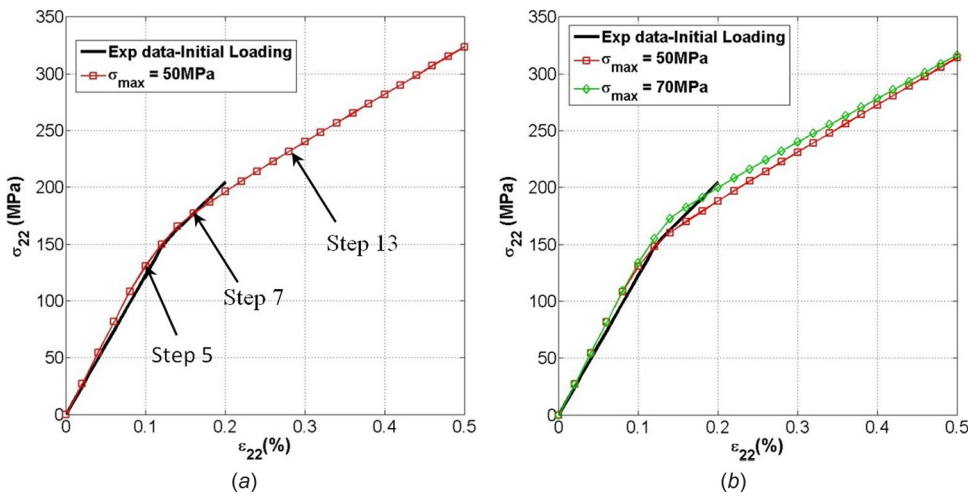


Fig. 10 Initial transverse response of the unidirectional SiC/Ti composite immediately after fabrication cooldown, illustrating the effect of (a) uncoupled and (b) coupled interfacial separation laws

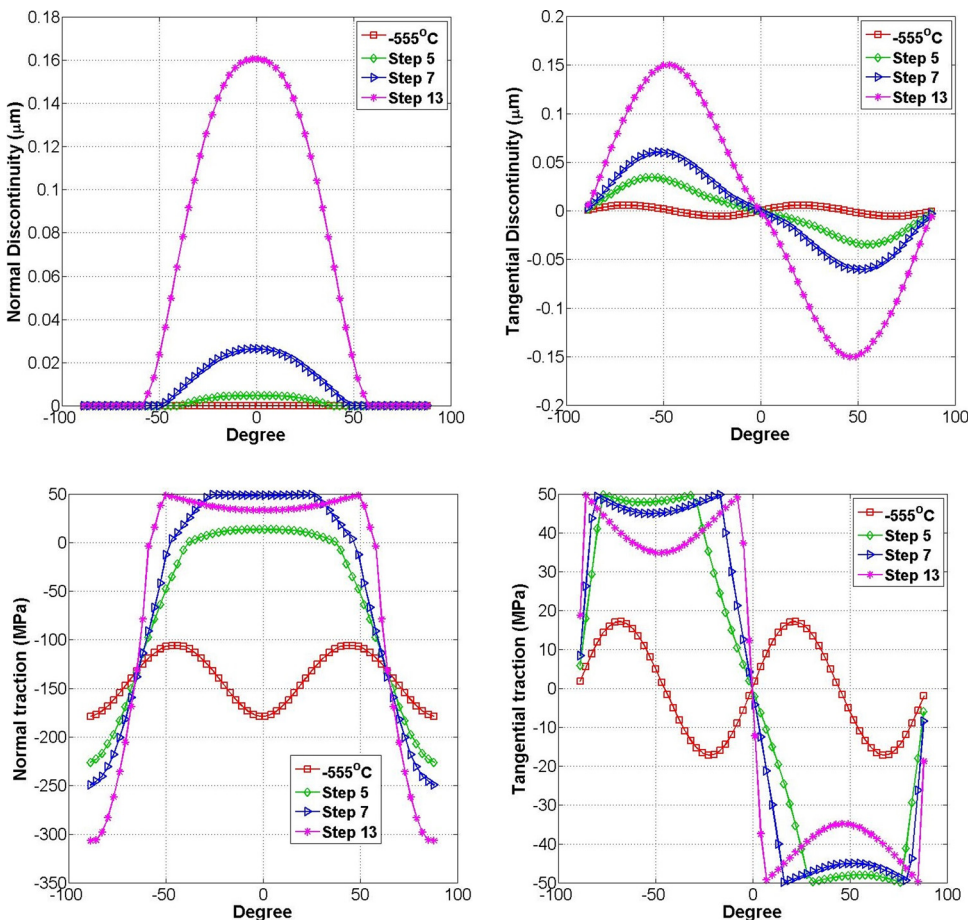


Fig. 11 Interfacial displacement discontinuity and traction distributions around the fiber/matrix interface with progressively greater applied load after fabrication cooldown

a number of factors that are beyond this paper's scope, including deviation from periodicity in the actual composite leading to unsymmetric fiber/matrix separation.

Next, we examine the evolution of normal and tangential displacement discontinuities and tractions around the fiber/matrix interface and the corresponding stress field alterations at the different loading steps shown in Fig. 10 for the uncoupled separation

law. Figure 11 summarizes the distributions of normal and tangential displacement discontinuities and the corresponding tractions around the fiber/matrix interface, measured counterclockwise from the horizontal axis passing through the fiber's center, after the 555°C cooldown and at the subsequent mechanical loading steps 5, 7, and 13. During the cooldown cycle, neither interfacial normal opening nor tangential degradation occurs because the

radial stress at the fiber/matrix interface is negative while the tangential stress does not exceed the interfacial shear strength. Hence, the response remains linearly elastic. The normal interfacial tractions attain their maximum values at ± 45 deg locations in the considered ± 90 deg range due to the use of the square fiber array for the SiC/Ti composite. At these locations, the tangential tractions are zero while their maximum values occur at -67.5 deg and $+22.5$ deg. During subsequent mechanical loading, these locations are altered.

In order to initiate normal interfacial separation, the compressive residual radial stress must be overcome, which occurs between steps 4 and 5 at 0 deg and is followed by interfacial elastic deformation until step 7 at which point the peak interfacial normal stress is attained along substantial portion of the interface spanning approximately ± 25 deg. Increasing loading produces increasing interfacial degradation accompanied by increasing normal separation characterized by increasing arc length and decreasing normal traction seen at step 13. The process is somewhat different for interfacial separation in the tangential direction. The interfacial sliding initiates much earlier (almost immediately after the cooldown), so that the interfacial shear strength is attained at step 4 (not shown). Hence, at step 5, the interfacial shear separation is substantially larger in magnitude than the corresponding normal separation. These differences tend to disappear with increasing load as seen at step 13. Similar behavior is observed in the traction distributions after the interface degrades. The important phenomenon that occurs with increasing loading, which may be deduced from the above results, is the eventual arrest of the

separation zone progression due to rapidly decreasing normal and tangential tractions outside of the separated zones around the fiber/matrix interface. This occurs at approximately ± 55 deg and $\pm [85 \text{ deg}/10 \text{ deg}]$ for the normal and tangential displacement discontinuities, respectively. In fact, the normal traction becomes compressive outside of the ± 55 deg interval while the shear traction tends to zero outside of the $\pm [85 \text{ deg}/10 \text{ deg}]$ intervals.

We end this section by presenting the full-field stress distributions in Fig. 12 at the loading steps shown in Fig. 10, including the three inplane stresses, σ_{22} , σ_{33} , and σ_{23} , and the effective stress σ_{eff} , which provides indication of yielding. These stress distributions demonstrate that the stress transfer mechanism from the region of the damage interface to the surrounding matrix is correctly captured by the implemented CZM into the FVDAM framework with fidelity comparable to an elasticity solution. In particular, as the interface loses its load-bearing capability, the matrix picks up a disproportionate portion of the applied horizontal load. We note that the effective yield stress at step 13 locally exceeds the yield stress of this particular titanium alloy in a small region at the apex of the fiber, requiring consideration of plasticity effects beyond this load step.

4.2 Progressive Interfacial Degradation After Initial Preload Cycles.

Initial loading cycles performed by Johnson et al. [43] on the unidirectional SiC/Ti composite produced observable fiber/matrix separation of a certain length around the interface, effectively resulting in destruction of the chemical fiber/

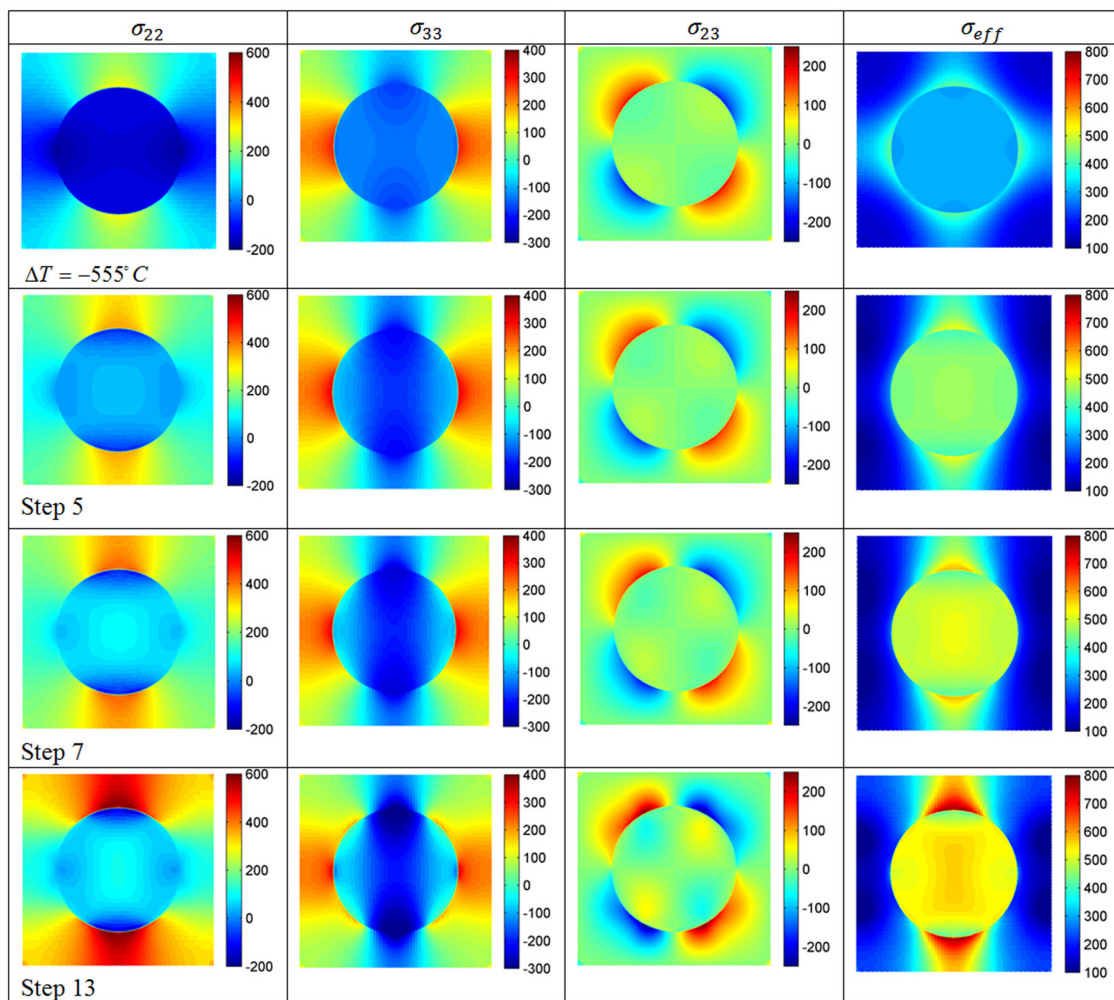


Fig. 12 Full-field stress distributions at progressively greater applied load after fabrication cooldown

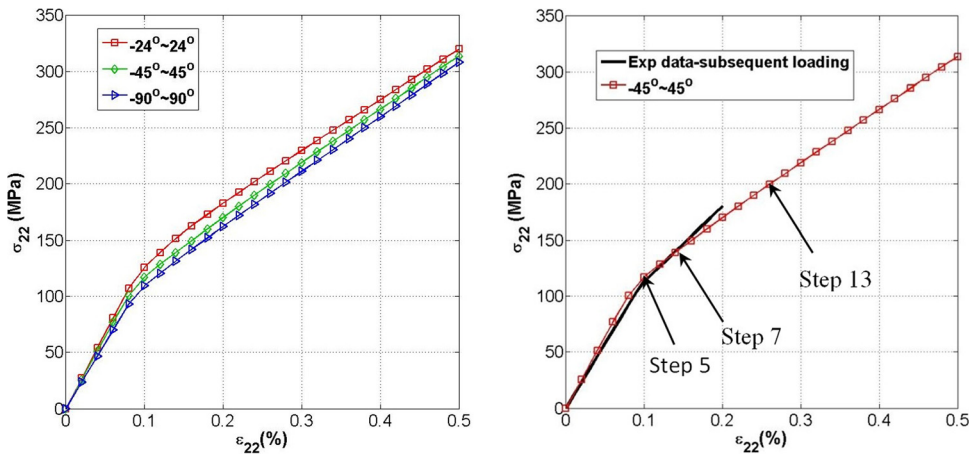


Fig. 13 Transverse response of the representative unit cell of unidirectional SiC/Ti composite with different interfacial debonding lengths after initial preloading

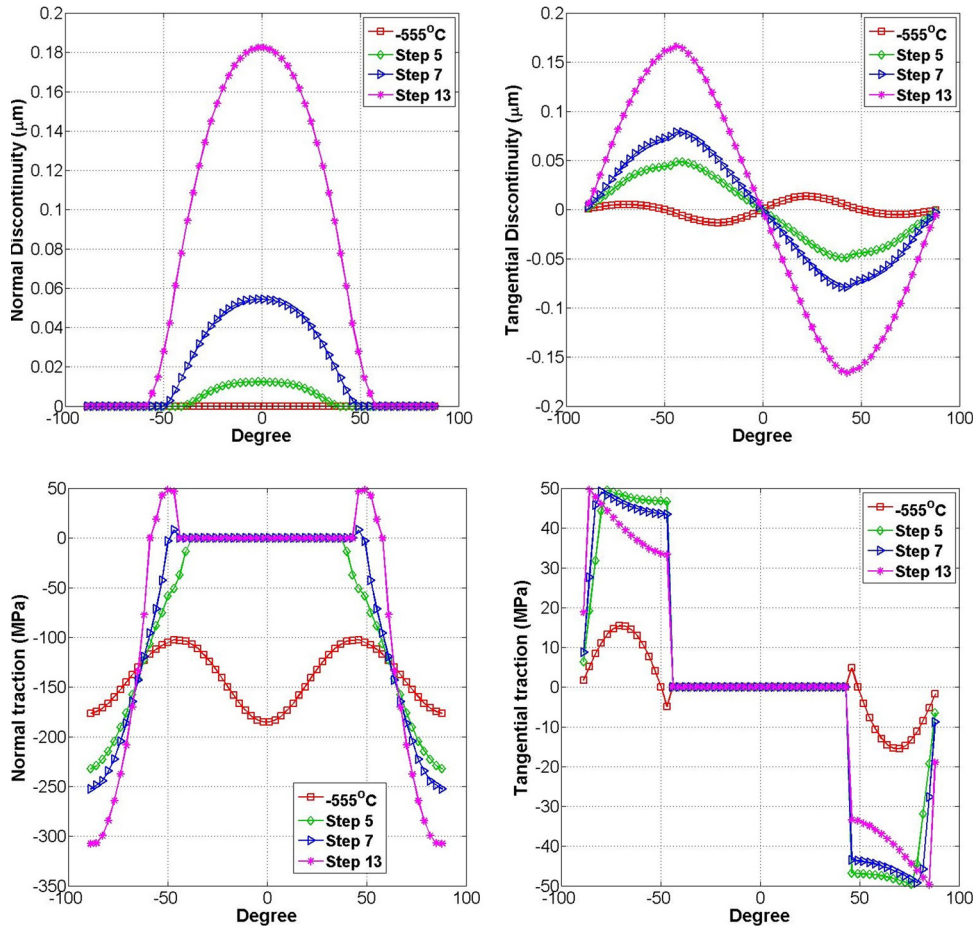


Fig. 14 Interfacial displacement discontinuity and traction distributions around the fiber/matrix interface with progressively greater applied load after initial preloading

matrix bond in that region. The extent of this damage, that is the arc length of the interface that was damaged and the corresponding applied load, however, was not reported. Simulation of the subsequent response after initial preload cycles requires knowledge of the extent of this damage which has a substantial effect on the homogenized response. This is illustrated in Fig. 13 for different lengths of damaged interface relative to the interface that is completely damaged around the entire circumference of the fiber.

In performing these simulations, the traction-free condition in the damaged region was employed in the auxiliary system of equations used to solve the unit cell problem, while outside this region the interfacial separation law was applied. In the present case, the best correlation with experiment was obtained when the damage to the fiber/matrix interface caused by cyclic loading spans $\pm 45^\circ$ deg relative to the horizontal axis as also observed in Fig. 13. This length is consistent with the results of Fig. 11 which suggest

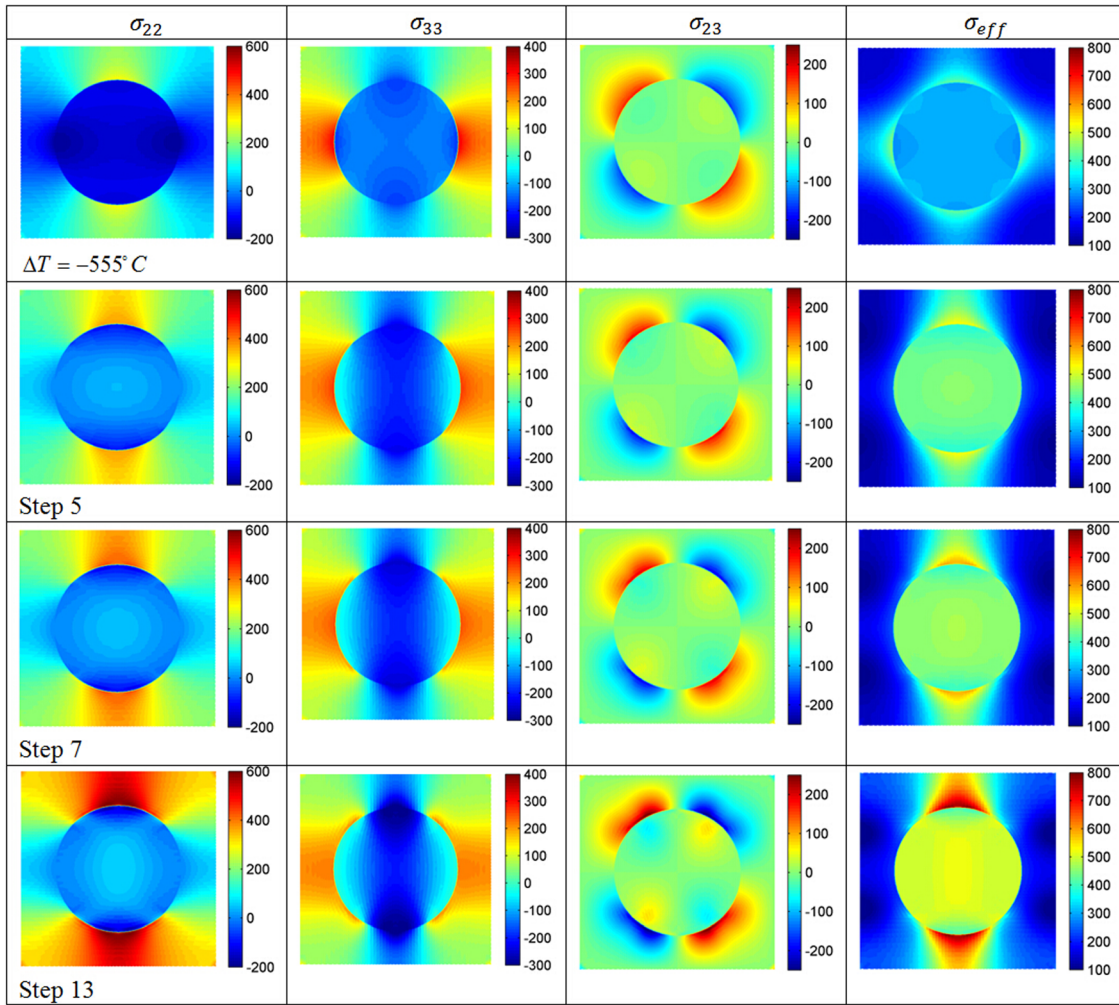


Fig. 15 Full-field stress distributions at progressively greater applied load after fiber/matrix degradation by initial preloading

that the maximum length of the fully degraded interface cannot exceed ± 55 . In fact, it is likely less than ± 50 given that the maximum normal traction that the interface can support at the onset of degradation does not extend beyond this region.

Figure 14 illustrates the distributions of normal and tangential displacement discontinuities and corresponding tractions around the fiber/matrix interface at the same subsequent loading steps used in Sec. 4.1 in the presence of intact interface after fabrication cooldown, namely, 5, 7, and 13 which are also indicated in Fig. 13. At step 5, the compressive radial stress is already overcome in the damaged region and the matrix separates from the fiber along the entire ± 45 deg arc segment of the interface. The normal traction becomes zero in the separated region and negative outside. With the increase in loading, the magnitude of the normal displacement discontinuity increases and the fiber/matrix interfacial segment undergoing separation progresses further along the fiber's circumference. As expected, the displacement discontinuities at each load step are greater in this case relative to the initially intact interface simulations of Sec. 4.1, Fig. 11, due to the absence of normal traction which constrains the interfacial separation. The interfacial zone progression is accompanied by an increase in the normal traction outside of the zero-traction region that drives further separation and degradation as the normal traction reaches the interfacial strength. As in the preceding case, the interfacial separation process is arrested around ± 55 deg as the normal traction decreases rapidly to a negative value outside of the separated zone. The tangential displacement discontinuity and traction distributions follow a similar pattern

but the maximum values are attained much earlier as also observed in the preceding case.

Figure 15 illustrates the full-field distributions of the three inplane stresses σ_{22} , σ_{33} , and σ_{23} , and the effective stress σ_{eff} for comparison with those of Fig. 12 with the initially intact interface. The rapid opening of the damaged interface once the compressive residual stresses are overcome renders the matrix material directly in front of the separated traction-free interface not as effective in supporting the applied horizontal load, producing lower magnitudes of the σ_{22} stress component. This is accompanied by visibly lower magnitudes of the σ_{33} stress component in this region due to the reduced constraint of the separated interface.

5 Discussion

The generated results demonstrate that the zeroth-order version of the parametric FVDAM theory is capable of accurately capturing interfacial displacement discontinuity and corresponding traction distributions along interfaces undergoing separation based on the bilinear CZM. In this version, only the continuity of interfacial surface-averaged displacements and tractions is enforced, in contrast with recently developed generalized version wherein additional higher-order kinematic and static interfacial variables are also employed producing nearly perfect interfacial conformability in the absence of damage [46]. Such capability may be important in problems undergoing very large deformations not pursued herein.

The present framework, based on the local/global stiffness matrix approach and the decomposition of interfacial displacements into continuous and discontinuous contributions, provides substantial flexibility in simulating interfacial degradation in heterogeneous materials, as well as other related phenomena. The auxiliary system of equations that governs the interfacial response admits arbitrary interfacial traction-separation laws, including CZM equations employed in the present study. Because the auxiliary equations may be activated by problem-specific conditions, various physical phenomena that may arise at different points along the loading path may be simulated using this approach. This is similar to the on-demand insertion of interface elements within the finite-element framework proposed by Ortiz and Suresh [6], which the present framework enables naturally.

It is also significant that physically realistic interfacial parameters were identified that produced good correlation with the reported experimental response of unidirectional SiC/Ti composite. Specifically, the employed maximum interfacial separation distance of $0.46\text{ }\mu\text{m}$ corresponding to traction-free interface compares well with the SiC fiber diameter of $146\text{ }\mu\text{m}$ and the thickness of the chemically degraded fiber/matrix interfacial zone that leads to premature separation under low transverse load. This is in contrast with the wide range of interfacial parameters found in the literature, some of which may be unrealistic as reported by Chandra et al. [37]. Identification of realistic interfacial strength parameters may be accomplished by incorporating the CZM-based FVDAM theory into an optimization algorithm, as recently demonstrated by Tu and Pindera [47] in the context of bio-inspired microstructures using the particle swarm optimization of Kennedy and Eberhart [48]. Similar capability was developed in the present context in search of optimal values for the interfacial strength and stiffness by allowing these quantities to vary in the ranges of $20\text{--}140\text{ MPa}$ and $1000\text{--}10,000\text{ MPa}/\mu\text{m}$, respectively. Optimal values of 58.5 MPa for the interfacial strength and $1090\text{ MPa}/\mu\text{m}$ for the initial interfacial stiffness were found that improved the correlation with experiment relative to the predictions based on the best values given in Table 3. Details of this combined PSO-FVDAM optimization capability facilitated by the semi-analytical structure of the FVDAM theory will be reported elsewhere.

6 Summary and Conclusions

The parametric FVDAM theory has been further extended in order to accommodate damage evolution based on displacement discontinuity functions. Auxiliary equations that represent traction conditions along specified interfaces undergoing separation, which are necessary to determine these functions, may be based either on traction-free conditions that simulate crack growth or interfacial separation laws based on the flexible interface concept. Herein, the CZM has been implemented into the auxiliary equations to simulate progressive damage between adjacent phases within the representative unit cell of a periodic material. The implemented CZM has been verified in the linear elastic region upon comparison with a modified Eshelby solution, which accounts for a flexible interface between the fiber and matrix phases. Both the interfacial separations and tractions around the interface and the full-field stress distributions have been captured by the extended FVDAM with fidelity comparable to the elasticity solution. Subsequently, the extended FVDAM theory was employed to study progressive damage around the fiber/matrix interface of a unidirectional SiC/Ti material subjected to transverse loading. Consistent CZM parameters have been identified that produced very good correlation with the reported experimental response immediately after fabrication cooldown when the interface was assumed intact, as well as after several cycles which destroyed the chemical bond along a portion of the interface. Examination of the evolution of interfacial displacement discontinuities and tractions with increasing load revealed that the extended FVDAM theory with CZM-based damage evolution

capability correctly captured the mechanics of progressive interfacial debonding, with the concomitant local stress fields exhibiting fidelity comparable to an elasticity solution.

Acknowledgment

The authors acknowledge the support of the Civil and Environmental Engineering Department at the University of Virginia through a teaching assistantship to the lead author.

References

- [1] Barenblatt, G. I., 1959, "The Formation of Equilibrium Cracks During Brittle Fracture. General Ideas and Hypothesis. Axially-Symmetric Cracks," *Prikl. Mat. Mekh.*, **23**(3), pp. 434–444.
- [2] Barenblatt, G. I., 1962, *Mathematical Theory of Equilibrium Cracks in Brittle Fracture* (Advances in Applied Mechanics, Vol. VII), H. L. Dryden, and T. von Karman, eds., Academic, New York, pp. 55–125.
- [3] Dugdale, D. S., 1960, "Yielding of Steel Sheets Containing Slits," *J. Mech. Phys. Solids*, **8**(2), pp. 100–104.
- [4] Needleman, A., 1987, "A Continuum Model for Void Nucleation by Inclusion Debonding," *ASME J. Appl. Mech.*, **54**(3), pp. 525–531.
- [5] Xu, X. P., and Needleman, A., 1994, "Numerical Simulation of Fast Crack Growth in Brittle Solids," *J. Mech. Phys. Solids*, **42**(9), pp. 1397–1434.
- [6] Ortiz, M., and Suresh, S., 1993, "Statistical Properties of Residual Stresses and Intergranular Fracture in Ceramic Materials," *ASME J. Appl. Mech.*, **60**(1), pp. 77–84.
- [7] Camacho, G. T., and Ortiz, M., 1996, "Computational Modeling of Impact Damage in Brittle Materials," *Int. J. Solids Struct.*, **33**(20–22), pp. 2899–2938.
- [8] Elices, M., Guinea, G. V., Gomerz, J., and Planas, J., 2002, "The Cohesive Zone Model: Advantages, Limitations and Challenges," *Eng. Fract. Mech.*, **69**(2), pp. 137–163.
- [9] Jiang, L. Y., Tan, H. L., Wu, J., Huang, Y. G., and Hwang, K. C., 2007, "Continuum Modeling of Interfaces in Polymer Matrix Composites Reinforced by Carbon Nanotubes," *Nano*, **2**(3), pp. 139–149.
- [10] Banea, M. D., and da Silva, L. F. M., 2009, "Adhesively Bonded Joints in Composite Materials: An Overview," *Proc. Inst. Mech. Eng.*, Part L, **223**, pp. 1–18.
- [11] Kim, Y. P., 2011, "Cohesive Zone Model to Predict Fracture in Bituminous Materials and Asphaltic Pavements: State-of-the-Art Review," *Int. J. Pavement Eng.*, **12**(4), pp. 343–356.
- [12] Park, K., and Paulino, G. H., 2011, "Cohesive Zone Models: A Critical Review of Traction-Separation Relationships Across Fracture Surfaces," *ASME Appl. Mech. Rev.*, **64**(6), p. 060802.
- [13] Beregovski, A., Engelbrecht, J., and Maugin, G. A., 2008, *Numerical Simulation of Waves and Fronts in Inhomogeneous Solids, Series A*, Vol. 62, World Scientific, Hackensack, NJ.
- [14] Versteeg, H. K., and Malalasekera, W., 2007, *An Introduction to Computational Fluid Dynamics: The Finite Volume Method*, Pearson Education, Ltd., Prentice-Hall, New York.
- [15] Ivankovic, A., Demirdzic, I., Williams, J. G., and Levers, P. S., 1994, "Application of the Finite Volume Method to the Analysis of Dynamic Fracture Problems," *Int. J. Fract.*, **66**(4), pp. 357–371.
- [16] Ivankovic, A., 1999, "Finite Volume Modelling of Dynamic Fracture Problems," *Comput. Model. Simul. Eng.*, **4**, pp. 227–235.
- [17] Stylianou, V., and Ivankovic, A., 2002, "Finite Volume Analysis of Dynamic Fracture Phenomena, Part II: A Cohesive Zone Type Modelling," *Int. J. Fract.*, **113**(2), pp. 107–123.
- [18] Karac, A., Blackman, B. R. K., Cooper, V., Kinloch, A. J., Sanchez, S. R., Teo, W. S., and Ivankovic, A., 2011, "Modelling the Fracture Behaviour of Adhesively-Bonded Joints as a Function of Test Rate," *Eng. Fract. Mech.*, **78**(6), pp. 973–989.
- [19] Carolan, D., Tukovic, Z., Murphy, N., and Ivankovic, A., 2013, "Arbitrary Crack Propagation in Multi-Phase Materials Using the Finite Volume Method," *J. Comput. Mater. Sci.*, **69**, pp. 153–159.
- [20] Cavalcante, M. A. A., Pindera, M.-J., and Khatam, H., 2012, "Finite-Volume Micromechanics of Periodic Materials: Past, Present and Future," *Composites, Part B*, **43**(6), pp. 2521–2543.
- [21] Pindera, M.-J., Khatam, H., Drago, A. S., and Bansal, Y., 2009, "Micromechanics of Spatially Uniform Heterogeneous Media: A Critical Review and Emerging Approaches," *Composites, Part B*, **40**(5), pp. 349–378.
- [22] Tukovic, Z., Ivankovic, A., and Karac, A., 2013, "Finite-Volume Stress Analysis in Multi-Material Linear Elastic Body," *Int. J. Numer. Meth. Eng.*, **93**(4), pp. 400–419.
- [23] Alveen, P., McNamara, D., Carolan, D., Murphy, N., and Ivankovic, A., 2014, "Analysis of Two-Phase Ceramic Composites Using Micromechanical Models," *Comput. Mater. Sci.*, **92**, pp. 318–324.
- [24] Chen, L., and Pindera, M.-J., 2007, "Plane Analysis of Finite Multilayered Media With Multiple Aligned Cracks. Part I: Theory," *ASME J. Appl. Mech.*, **74**(1), pp. 128–143.
- [25] Cavalcante, M. A. A., Marques, S. P. C., and Pindera, M.-J., 2007, "Parametric Formulation of the Finite-Volume Theory for Functionally Graded Materials. Part I: Analysis," *ASME J. Appl. Mech.*, **74**(5), pp. 935–945.
- [26] Bansal, Y., and Pindera, M.-J., 2003, "Efficient Reformulation of the Thermoelastic Higher-Order Theory for Functionally Graded Materials," *J. Therm. Stresses*, **26**(11/12), pp. 1055–1092.

- [27] Gattu, M., Khatam, H., Drago, A. S., and Pindera, M.-J., 2008, "Parametric Finite-Volume Micromechanics of Uniaxial, Continuously-Reinforced Periodic Materials With Elastic Phases," *ASME J. Eng. Mater. Technol.*, **130**(3), p. 031015.
- [28] Khatam, H., and Pindera, M.-J., 2009, "Thermo-Elastic Moduli of Lamellar Composites With Wavy Architectures," *Composites, Part B*, **40**(1), pp. 50–64.
- [29] Khatam, H., and Pindera, M.-J., 2009, "Parametric Finite-Volume Micromechanics of Periodic Materials With Elastoplastic Phases," *Int. J. Plast.*, **25**(7), pp. 1386–1411.
- [30] Bansal, Y., and Pindera, M.-J., 2005, "A Second Look at the Higher-Order Theory for Periodic Multiphase Materials," *ASME J. Appl. Mech.*, **72**(2), pp. 177–195.
- [31] Bansal, Y., and Pindera, M.-J., 2006, "Finite-Volume Direct Averaging Micromechanics of Heterogeneous Materials With Elastic-Plastic Phases," *Int. J. Plast.*, **22**(5), pp. 775–825.
- [32] Bensoussan, A., Lions, J.-L., and Papanicolaou, G., 1978, *Asymptotic Analysis for Periodic Structures*, North Holland, Amsterdam, Netherlands.
- [33] Suquet, P. M., 1987, *Elements of Homogenization for Inelastic Solid Mechanics* (Lecture Notes in Physics, Vol. 272), Springer-Verlag, Berlin, pp. 193–278.
- [34] Charalambakis, N., 2010, "Homogenization Techniques and Micromechanics. A Survey and Perspectives," *ASME Appl. Mech. Rev.*, **63**(3), p. 0308031.
- [35] Achenbach, J. D., 1975, *A Theory of Elasticity With Microstructure for Directionally Reinforced Composites*, Springer-Verlag, New York.
- [36] Geubelle, P. H., and Baylor, J. S., 1998, "Impact-Induced Delamination of Composites: A 2D Simulation," *Composites, Part B*, **29**(5), pp. 589–602.
- [37] Chandra, N., Li, H., Shet, C., and Ghonem, H., 2002, "Some Issues in the Application of Cohesive Zone Models for Metal–Ceramic Interfaces," *Int. J. Solids Struct.*, **39**(10), pp. 2827–2855.
- [38] Matous, K., and Geubelle, P. H., 2006, "Multiscale Modelling of Particle Debonding in Reinforced Elastomers Subjected to Finite Deformations," *Int. J. Numer. Meth. Eng.*, **65**(2), pp. 190–223.
- [39] Song, S. H., Paulino, G. H., and Buttlar, W. G., 2006, "A Bilinear Cohesive Zone Model Tailored for Fracture of Asphalt Concrete Considering Viscoelastic Bulk Material," *Eng. Fract. Mech.*, **73**(18), pp. 2829–2848.
- [40] Hill, R., 1963, "Elastic Properties of Reinforced Solids: Some Theoretical Principles," *J. Mech. Phys. Solids*, **11**(5), pp. 357–372.
- [41] Eshelby, J. D., 1957, "The Determination of the Elastic Field of an Ellipsoidal Inclusion and Related Problems," *Proc. R. Soc., London, Ser. A*, **241**(1226), pp. 376–396.
- [42] Drago, A. S., and Pindera, M.-J., 2008, "A Locally Exact Homogenization Theory for Periodic Microstructures With Isotropic Phases," *ASME J. Appl. Mech.*, **75**(5), p. 051010.
- [43] Johnson, W. S., Lubowinski, S. J., and Highsmith, A. L., 1990, "Mechanical Characterization of Unnotched SCS6/Ti-15-3 Metal Matrix Composites at Room Temperature, Thermal and Mechanical Behavior of Metal Matrix and Ceramic Matrix Composites," J. M. Kennedy, H. H. Moeller, W. S. Johnson, eds., American Society for Testing and Materials, Philadelphia, PA, pp. 193–218, Paper No. ASTM STP 1080.
- [44] Dieter, G. E., 1976, *Mechanical Metallurgy*, 2nd ed., McGraw-Hill, New York, pp. 451–489.
- [45] Raghavan, P., and Ghosh, S., 2005, "A Continuum Damage Mechanics Model for Unidirectional Composites Undergoing Interfacial Debonding," *Mech. Mater.*, **37**(9), pp. 955–979.
- [46] Cavalcante, M. A. A., and Pindera, M.-J., 2014, "Generalized FVDAM Theory for Periodic Materials Undergoing Finite Deformation. Part I: Framework," *ASME J. Appl. Mech.*, **81**(2), p. 021005.
- [47] Tu, W., and Pindera, M.-J., 2013, "Targeting the Finite-Deformation Response of Wavy Biological Tissues With Bio-Inspired Material Architectures," *J. Mech. Behav. Biomed. Mater.*, **28**, pp. 291–308.
- [48] Kennedy, J., and Eberhart, R., 1995, "Particle Swarm Optimization," *IEEE International Conference on Neural Networks*, Perth, WA, November 27–December 1, pp. 1942–1948.